LBL-34832
UC-404

Lawrence Berkeley Laboratory

UNIVERSITY OF CALIFORNIA

Engineering Division

Potassium Dihydrogen Phosphate and Potassium Tantalate Niobate Pyroelectric Materials and Far-Infrared Detectors

H.B. Baumann
(M.S. Thesis)

October 1993

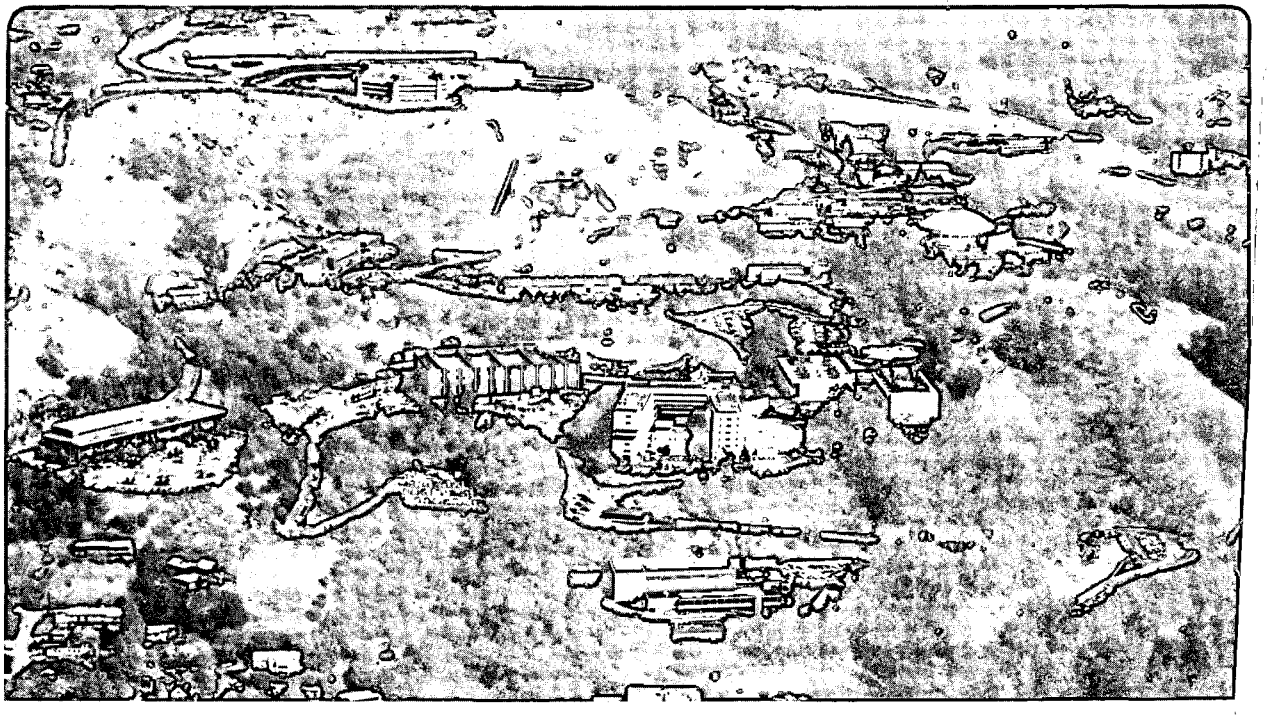

LOAN COPY
Circulates
for 4 weeks
Bldg. 50 Library.
Copy 2
LBL-34832

Prepared for the U.S. Department of Energy under Contract Number DE-AC03-76SF00098

DISCLAIMER

This document was prepared as an account of work sponsored by the United States Government. Neither the United States Government nor any agency thereof, nor The Regents of the University of California, nor any of their employees, makes any warranty, express or implied, or assumes any legal liability or responsibility for the accuracy, completeness, or usefulness of any information, apparatus, product, or process disclosed, or represents that its use would not infringe privately owned rights. Reference herein to any specific commercial product, process, or service by its trade name, trademark, manufacturer, or otherwise, does not necessarily constitute or imply its endorsement, recommendation, or favoring by the United States Government or any agency thereof, or The Regents of the University of California. The views and opinions of authors expressed herein do not necessarily state or reflect those of the United States Government or any agency thereof or The Regents of the University of California and shall not be used for advertising or product endorsement purposes.

Lawrence Berkeley Laboratory is an equal opportunity employer.

This publication has been reproduced from the best available copy

DISCLAIMER

This document was prepared as an account of work sponsored by the United States Government. While this document is believed to contain correct information, neither the United States Government nor any agency thereof, nor the Regents of the University of California, nor any of their employees, makes any warranty, express or implied, or assumes any legal responsibility for the accuracy, completeness, or usefulness of any information, apparatus, product, or process disclosed, or represents that its use would not infringe privately owned rights. Reference herein to any specific commercial product, process, or service by its trade name, trademark, manufacturer, or otherwise, does not necessarily constitute or imply its endorsement, recommendation, or favoring by the United States Government or any agency thereof, or the Regents of the University of California. The views and opinions of authors expressed herein do not necessarily state or reflect those of the United States Government or any agency thereof or the Regents of the University of California.

LBL - 34832

POTASSIUM DIHYDROGEN PHOSPHATE AND POTASSIUM TANTALATE NIOBATE PYROELECTRIC MATERIALS AND FAR-INFRARED DETECTORS

HILARY BEATRIX BAUMANN

MATERIALS SCIENCE AND MINERAL ENGINEERING DEPARTMENT
University of California
Berkeley, CA 94720

and

ENGINEERING DIVISION
Lawrence Berkeley Laboratory
Berkeley, CA 94720

M.S. Thesis

October 1993

This work was supported by NASA Contract No. A59513C through interagency agreement with the U.S. Department of Energy under Contract No. DE-AC03-76SF00098.

recycled paper

TABLE OF CONTENTS

Acknowledgements

1 Introduction 1

2 Pyroelectric Materials
2.1 Dielectric Properties 4
2.2 Spontaneous Polarization 7
2.3 Ferroelectrics
2.3.1 Domains 9
2.3.2 Curie Temperature 12

3 Pyroelectric Detectors
3.1 Pyroelectric Current 16
3.2 Responsivity 17
3.3 Noise 22
3.4 Radiation Absorption 25

4 Materials
4.1 Properties and Selection Criteria 27
4.2 Potassium Dihydrogen Phosphate (KDP) 28
4.3 Potassium Tantalate Niobate (KTN) 39

5 Sample Preparation
5.1 KDP 31
5.2 KTN 35

6 Detector Configuration
6.1 Detector Mount 37
6.2 Thermal Analysis 39
6.3 Absorbing Layer 45

7 Electrical Characterization
7.1 Capacitance Measurements 47
7.2 Response Measurements 56

8 Conclusions 62

9 References 64

Appendices
A. Table of Crystal Classes 68
B. Thermal Conductivity of Wire 69
C. Specific Heat of KDP 70
D. Capacitance Bridge 71

ACKNOWLEDGEMENTS

Most of all I thank Professor Eugene Haller for providing me with the opportunity to pursue this research. I am especially appreciative of the knowledge, patience and support he has displayed toward my project. Special thanks are extended to Jeff Atherton and Eberhard Prochnow of the Advanced Lasers Group at Lawrence Livermore National Laboratory for providing high quality KDP crystals, to Dr. Daniel Rytz of the Optoelectronics Division of the Sandoz Corporation in France for donating crystalline KTN samples, and to Bob Hanel of NASA Ames Research Center for measuring the optical response of the pyroelectric devices. I am also grateful to Jeff Beeman, Howard Chang, Dick Davis, Bill Hansen, and Amy Moll who have all contributed to this project. In addition, I thank my parents, my brother Chris, Will Cherry, and the students and staff working in our group at Lawrence Berkeley Laboratory for their support and advice.

1. INTRODUCTION

In 1961 Hanel[1] fabricated the first dielectric bolometer. He irradiated a voltage biased ferroelectric capacitor near its Curie temperature with a chopped infrared (IR) source and measured a signal from the periodic change in its capacitance. Then in 1962 Cooper[2,3] derived the responsivity equation for a pyroelectric bolometer based on the pyroelectric effect. He subsequently demonstrated that a polarization change in ferroelectric barium titanate produces a signal.[4] Since then, pyroelectric detectors have been used in consumer products and scientific and military applications. Pyroelectric detectors are currently used in fire alarms, intruder detectors, gas analyzers, laser beam characterization, and thermal imaging.[5]

NASA's Earth Observing system needs broadband infrared detectors to meet new requirements for spaceborne sensors. These requirements are long-term stability, extended spectral range, minimal cooling, small and light support system, and low power consumption. Such IR detectors will also be useful for planetary exploration, space physics, the multi-agency Global Change program, and the Atmospheric Radiation Measurement program[6]. Pyroelectric detectors are expected to meet these new needs for both orbiting and planetary spacecraft. As bolometers, pyroelectric devices have a broad spectral response and are easily calibrated. In addition, existing pyroelectric materials can operate at temperatures around 100K. This temperature is realized on spacecraft by passive radiation cooling.[7] At 100K the thermal noise is substantially reduced from the room temperature thermal noise. Therefore, better performance is expected with pyroelectric detectors optimized to operate at 100K than with available room temperature pyroelectric detectors. Competing IR detectors such as mercury cadmium telluride photovoltaic devices operate below 85K requiring mechanical cooling systems. These

systems have limited operating lifetimes and increase the spacecraft mass and power consumption. In addition to the above attributes, pyroelectric detectors are simple to construct and operate, and do not require an external bias[8]. Operating ferroelectric detectors with a D.C. bias[9], however, increases the detector responsivity.[10,11]

Pyroelectric materials belong to the family of dielectric materials. Pyroelectrics are materials that posses a spontaneous polarization (or internal electric displacement) in the absence of an applied electric field or mechanical stress. The pyroelectric effect is the change in the spontaneous polarization with temperature, and results in corresponding changes in the surface charge of the pyroelectric material. Pyroelectric detectors are bolometers that take advantage of the pyroelectric effect to detect incident radiation. A pyroelectric bolometer is a capacitor made by depositing metal films on parallel and opposing faces of a thin slab of pyroelectric material. When the detector is connected to an electrical load, the heat from the incident radiation changes the internal polarization of the pyroelectric giving rise to a displacement current. This current flow is a measure of the temperature change and thus the rate of change of the incident radiation.

Ferroelectrics, a sub-class of pyroelectric materials, show domain formation with a distribution of polarization dipoles. Ferroelectrics are desired for thermal signal detection because they usually posses a large pyroelectric effect[12]. This effect is largest near the Curie temperature, T_c, of the ferroelectric. This thesis discusses the characterization of two ferroelectric materials and the fabrication of bolometers. Potassium tantalate niobate (KTN) and potassium dihydrogen phosphate (KDP) are chosen for detector materials because they can be optimized for operation near 100K. As an introduction, Chapter 2 reviews the physics underlying pyroelectric materials and its sub-

class of ferroelectric materials. Various aspects of pyroelectric detection are discussed in Chapter 3 including the measurement circuit, noise sources, and the effect of materials properties on the pyroelectric response. In Chapter 4 the selection of materials is discussed and the specific characteristics of KTN and KDP materials are given.

Chapter 5 describes the preparation of the KDP and KTN materials. In Chapter 6 the detector configuration is presented. In addition, a thermal analysis of the pyroelectric detector is performed. Electrical techniques used to characterize the ferroelectric materials and devices are described and results presented in Chapter 7. Conclusions are made about the feasibility of KDP and KTN pyroelectric detectors in Chapter 8.

2. PYROELECTRIC MATERIALS

2.1 Dielectric Properties

The dielectric permittivity is a measure of the polarization of a dielectric material in an electric field. Linear dielectrics polarize linearly with electric field while non-linear dielectrics do not. Pyroelectrics are non-linear dielectrics exhibiting spontaneous polarization; materials possessing spontaneous polarization are polar materials. The dielectric permittivity, ε, is related to the capacitance by the well-known capacitor equation:

$$C = \frac{\varepsilon\varepsilon_0 A}{d}. \qquad [2.1]$$

Non-polar dielectrics have a relative dielectric constant on the order of ε = 1-10. Pyroelectric dielectrics, on the other hand, exhibit a unique axis along which the relative dielectric constant may vary from $\varepsilon = 10\text{-}10^5$ upon application of an electric bias and/or change of temperature.[13]

The polarization of a dielectric material is the electric dipole moment per unit volume. An electric dipole results from the displacement of an electrically charged species within the material[14], as illustrated in Figure 2.1. In this case, the cations are displaced relative to the unit cell along line X leading to electric dipoles, or an electric dipole moment. The direction of the net polarization, **P**, is shown by the arrow. The amount of polarization depends on the magnitude and separation of charges. Polarization due to the displacement of bound ions with respect to one another, as described above, is called ionic polarization. There are three other mechanisms that contribute to polarization in materials: space charge, molecular polarization, and atomic polarization.

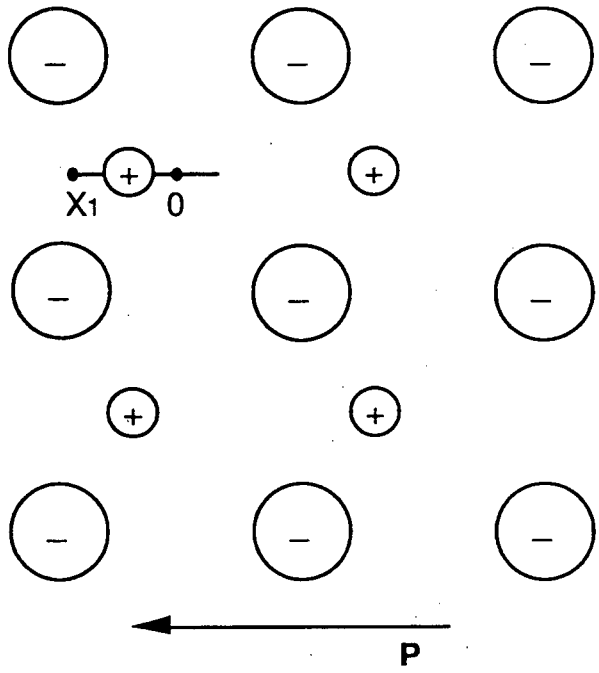

Figure 2.1. Schematic sketch of a two-dimensional electrically polar lattice (from Ref. 14). The large circles correspond to anions and the small circles represent cations. The cations are displaced along the X axis between 0 and X_1 resulting in a polarized lattice of polarization, **P**.

The frequency dependence of the dielectric constant arises from the time it takes for these various polarization mechanisms to develop. Space charge polarization is the slowest. It arises from the diffusion of ions over internal surfaces or grain boundaries on the order of many atomic spacings. It does not contribute to the polarization at frequencies greater than about 100Hz. Molecular dipoles respond to electric fields varying at frequencies up to about 10^8Hz. Ionic dipole response reaches about 10^{14}Hz. Atomic (or electronic) dipoles respond up to 10^{14}-10^{15}Hz. The frequency dependence of the polarization also gives rise to a time lag or phase difference (δ) between the externally applied alternating field and the internal polarization. When the

polarization is in phase with the frequency of the alternating field the dielectric is said to have zero loss. The loss is characterized by the dissipation factor,

$$\tan \delta = \frac{\varepsilon'}{\varepsilon''}, \qquad [2.2]$$

where $\varepsilon = \varepsilon' + i\varepsilon''$ is the complex dielectric constant. A "lossy" dielectric extracts energy from the electric field and produces heat.[15] The loss may be increased by domain boundary motion in ferroelectric crystals, and/or defects.[16]

The dielectric permittivity is a tensor,

$$\varepsilon_p = \frac{\mathbf{P}}{\mathbf{E}}, \qquad [2.3]$$

where $\varepsilon_p = \varepsilon\varepsilon_o$. Here ε_o is the permittivity of free space and, **P** and **E** are, respectively, the polarization and electric field in the same direction. The polarization of the crystal is the charge produced at the electrodes divided by the area (A),

$$P = \frac{q}{A}. \qquad [2.4]$$

The total polarization is often referred to as the electric displacement (**D**). Rewriting equation [2.3] the electric displacement is

$$\mathbf{D} = \varepsilon\varepsilon_o \mathbf{E} \qquad [2.5]$$

for a non-polar material. In addition to the electric field dependent polarization, polar materials spontaneously polarize. The electric displacement now becomes†

$$\mathbf{D} = \varepsilon\varepsilon_o \mathbf{E} + \mathbf{P_s} \qquad [2.6]$$

where $\mathbf{P_s}$ is the spontaneous polarization.

† The piezoelectric contribution to the electric displacement is not taken into consideration here.

Measurement of the dielectric constant is usually made using a weak electric field (10V/cm) in an A.C. bridge circuit.[17] If a significant D.C. bias is applied to the capacitor its dielectric properties may change dramatically. The dielectric constant of a linear dielectric has some upper limit of electric field, above which it becomes quickly non-linear and breaks down. The dielectric constant of non-linear dielectric material may be linear under weak electric fields, but becomes non-linear with the application of stronger fields. Non-linear dielectrics also have an electric field limit where they break down. In a plot of the electric displacement vs. electric field, the dielectric constant is the slope, as shown by Eq. [2.5]. For large electric fields, the plot is curved for non-linear materials and the slope, and thus the dielectric constant, varies.

2.2 Spontaneous Polarization

Spontaneous polarization, or the formation of spontaneous electric dipoles, arises from an asymmetry in the crystal structure with finite changes in temperature. Figure 2.2 shows the potential energy of the cation of Figure 2.1 in such an asymmetric environment. As the temperature is increased, the excitation of the cation to higher vibrational energy levels (parallel solid lines) causes displacement of its average equilibrium position (locus A-B) within the lattice along the X axis.[18] The change in position of the cation relative to the lattice results in spontaneous polarization. Since the spontaneous polarization arises from an asymmetric environment, it is understandable that pyroelectric crystals cannot belong to the cubic crystal system. The remaining 6 crystal systems all contain at least one crystal point group that is pyroelectric in nature. In all, there are 10 crystal classes that are pyroelectric[†]. (See the Table[19] in Appendix A for classification of different crystal systems and symmetry groups.)

[†] It is worthwhile to note that all pyroelectric materials are a subclass of piezoelectric materials.

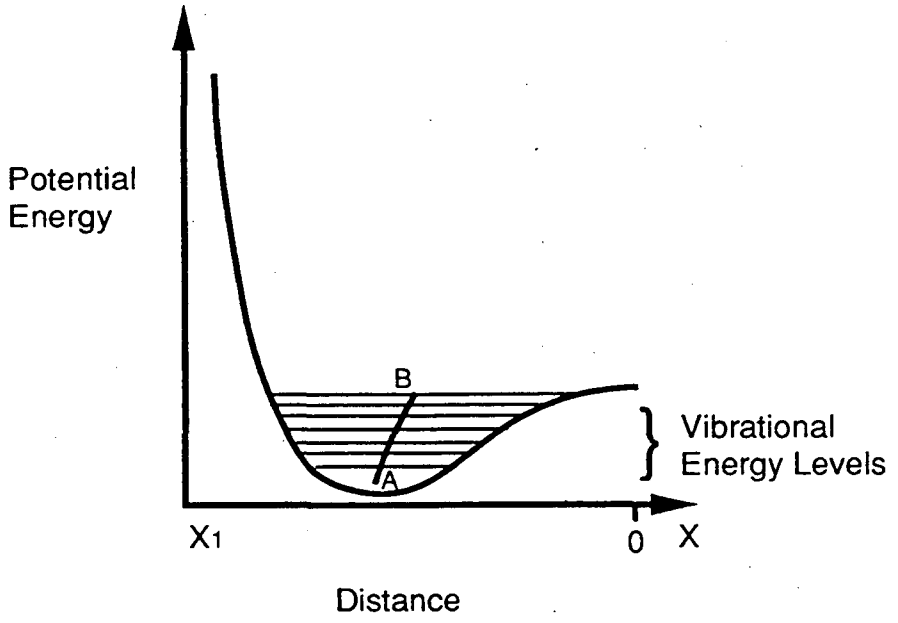

Figure 2.2. Potential energy of the cation as a function of position along X in the lattice of Figure 2.1 (from Ref. 18). The locus A-B is the change in the cation's mean equilibrium position with increasing temperature (vibrational energy).

Spontaneous polarization is not always observable in polar materials. The displacement and orientation of ions and charged molecular units takes a finite time.[20] Therefore, if the change in temperature occurs slowly, charge compensation of the dipoles occurs and the pyroelectric effect may not be observed. In conductors, compensation occurs when free charges within the crystal rearrange to neutralize the electric dipole. In insulators, free charges in the surrounding medium quickly flow to the surfaces to neutralize the electric dipole.[21] In addition, if there is more than one direction of the spontaneous polarization, as in ferroelectric and polycrystalline pyroelectrics[22], the opposing dipoles can cancel each other out to produce a zero net spontaneous polarization.

2.3 Ferroelectrics

2.3.1 Domains

Ferroelectric materials are a sub-class of pyroelectric materials. The spontaneous polarization of ferroelectrics has more than one orientation resulting in domains characterized by their polarization vectors. The directions of these polarization vectors, and thus domains, can be changed by an externally applied electric field.[23] The spontaneous polarization of most ferroelectrics is due to the formation of ionic dipoles[24]; molecular dipoles also produce spontaneous polarization. In ionic materials that spontaneously polarize, displacements of small, highly charged cations lead to large dipole moments. The closely spaced ions result in a strong dipole-dipole interaction.[25] To minimize their energy, neighbor dipoles polarize in the same direction. This leads to domains of uniform polarization analogous to the domains due to magnetic dipoles in ferromagnetic materials. The domain walls of ferroelectric materials are much narrower (1-2 atomic spacings) compared with the Bloch wall of ferromagnetic materials (750Å).[26] This is attributed to the larger anisotropic effect in ferroelectrics.[27] The orientations of these domains correspond to the unique polarization directions of the ferroelectric. Figure 2.3 a) shows a possible domain structure of single-crystal KH_2PO_4 (KDP). In KDP spontaneous polarization occurs in both directions along the c-axis in the orthorhombic phase resulting in domains oriented against each other by 180°. A material that exhibits spontaneous polarization in either direction along two perpendicular crystallographic axes exhibits 90° misoriented domains as shown in Figure 2.3 b).[28] Pyroelectric materials that can only spontaneously polarize in one direction along a unique polar axis, by definition, have only one domain and are not ferroelectric.

a) 180° Domains b) 90° Domains

2.3. Schematic of domains in ferroelectric crystals.

It is possible to reorient the domains with the application of an external electric field. The change in the polarization along a ferroelectric axis with electric field results in a hysteresis loop, as demonstrated by Figure 2.4. The hysteresis arises from a double potential well, shown in Figure 2.5, that the charged species experiences along the ferroelectric axis. Consider the ionic lattice in Figure 2.1 (Section 2.1), as an electric field is applied along the ferroelectric axis the cations move from one potential well (polarization) to the other. The polarization increases rapidly until all cations occupy the same potential well (saturation) and a linear regime takes over as in a linear dielectric. If the external electric field is reversed, the atoms return along the linear saturation region and then begin to switch from the current well to the other well, reversing the polarization. The hysteresis occurs because of the energy barrier between the two wells. In other words, there is an activation energy that must be overcome to reverse the polarization. The coercive electric field ($\mathbf{E_c}$) is the field at which polarization reversal occurs. The area within the hysteresis loop is a measure of the energy required to reverse the polarization twice. The spontaneous polarization ($\mathbf{P_s}$) and the remnant polarization ($\mathbf{P_r}$) are different if some of the dipoles reverse their polarization before the applied field reverses.[29]

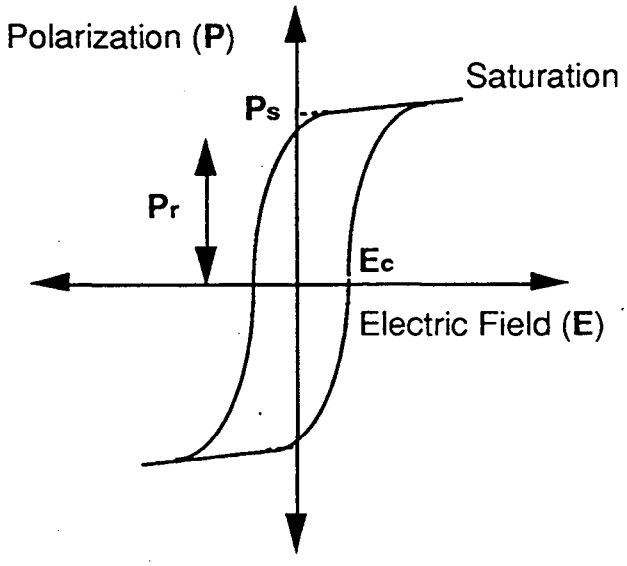

Figure 2.4. Polarization vs. electric field of a ferroelectric phase.

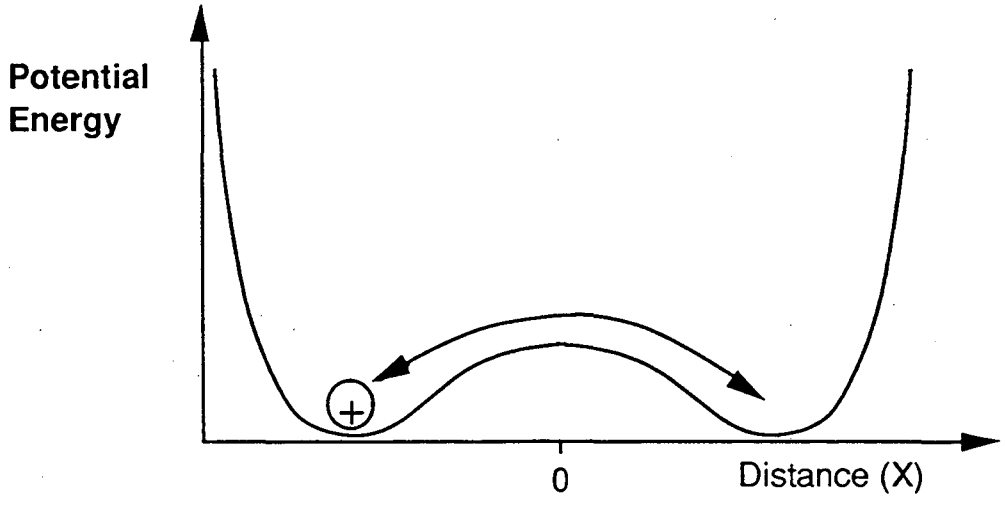

Figure 2.5. A double potential well experienced by charged specie along a ferroelectric axis (X).

2.3.2 Curie Temperature

Ferroelectric materials are characterized by a Curie temperature, T_C. The Curie temperature is the temperature at which a reversible phase transition occurs in the material. T_C is also referred to as the transition temperature. Typically, the material transforms from a high-temperature high-symmetry non-polar, or paraelectric, phase to a low-temperature, lower-symmetry ferroelectric phase. In many ferroelectrics, several ferroelectric phases exist, leading to ferroelectric–ferroelectric transitions. The highest temperature-stable phase compatible with the ferroelectric structure is deemed the prototype phase, and is usually cubic in structure. Some ferroelectrics, however, melt below the temperature at which the cubic phase becomes stable, resulting in a lower-symmetry prototype phase.[30]

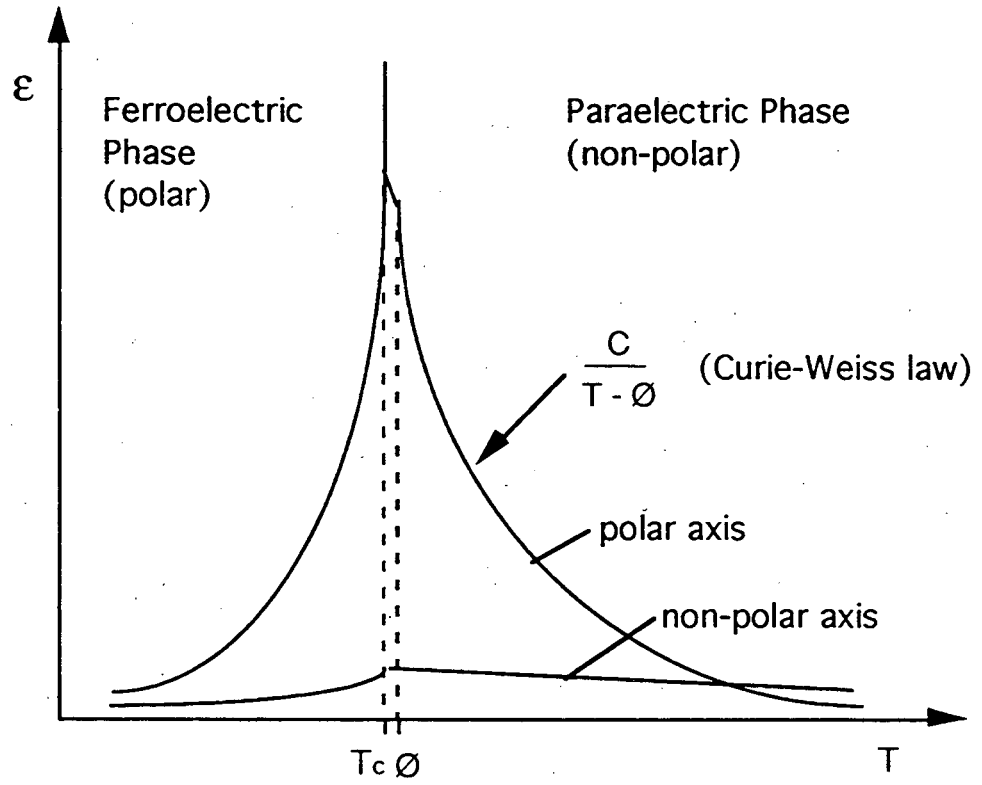

Figure 2.6. Dielectric permittivity vs. temperature of a polar and non-polar axis of a ferroelectric material (from Ref. 31).

Below T_C, in the ferroelectric phase, the material exhibits spontaneous polarization. This spontaneous polarization decreases as the Curie temperature is approached from below. The temperature at which the phase transformation occurs, T_C, is the temperature at which the spontaneous polarization falls to zero. In addition, these phase transformations are marked by an irregular peak in the dielectric constant along the polar axis at T_C. Figure 2.6. shows a plot of the dielectric permittivity vs. temperature across the transition temperature for a polar and non-polar axis of a ferroelectric crystal. Other anomalies occur in the piezoelectric, pyroelectric, and specific heat coefficients at T_C. Above the Curie temperature, in the non-polar (or paraelectric) phase, the dielectric constant obeys the equivalent of the Curie-Weiss behavior observed in ferromagnetic materials,

$$\varepsilon = \frac{C}{T - \varnothing} \qquad [2.7]$$

where C is the Curie constant. The Curie constant and the Curie-Weiss temperature, Ø, are unique to each ferroelectric transition; Ø and T_C may differ by as much as 10° C.[31]

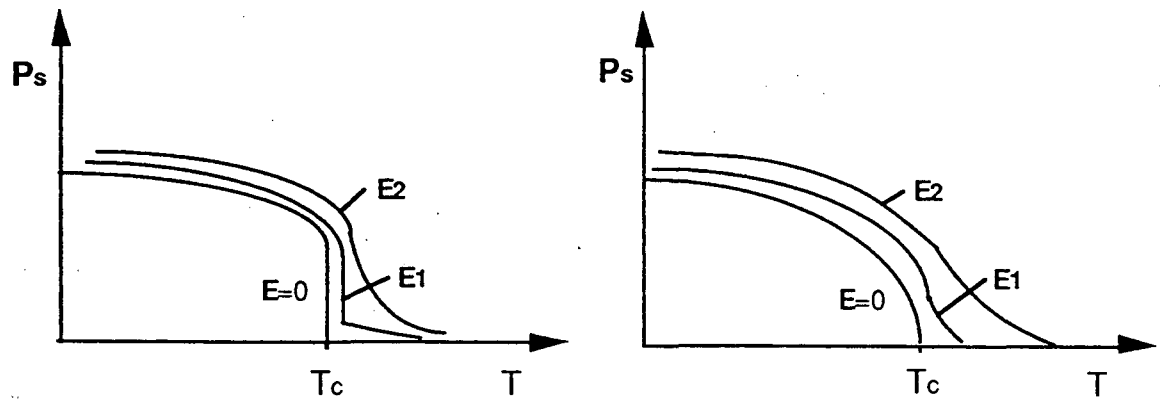

a) 1st-order phase transformation b) 2nd-order phase transformation

Figure 2.7. Spontaneous polarization vs. temperature and increasing bias, ($E_2 > E_1 > 0$).

The spontaneous polarization of the ferroelectric phase decreases and falls to zero at the Curie temperature, as shown in Figures 2.7 a) and b). The type of phase transformation influences the behavior of the spontaneous polarization near the Curie temperature. In a first-order transformation the spontaneous polarization changes discontinuously at the Curie temperature, while in a second-order transformation the spontaneous polarization changes more gradually as the Curie temperature is approached as illustrated in Figures 2.7 a) and b), respectively. For these figures, the crystals are non-polar above the Curie temperature resulting in a negative dP_s/dT. One ferroelectric has a positive dP_s/dT; Rochelle salt (sodium potassium tartrate) has a ferroelectric phase bounded by two non-polar phases.

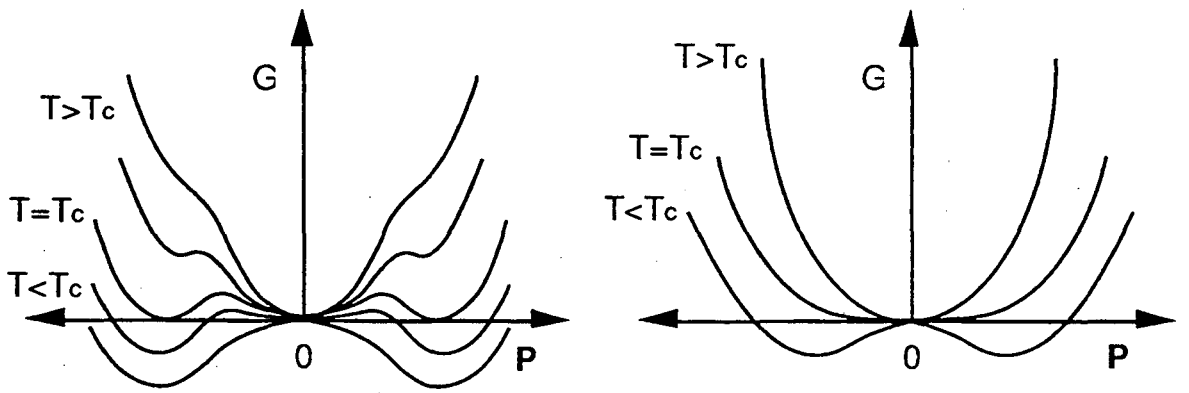

a) 1st-order phase transformation b) 2nd-order phase transformation

2.8. Free energy (**G**) vs. polarization (**P**)

In a first-order transition the onset of spontaneous polarization occurs more rapidly than in the second-order transition. The origin of this behavior is seen directly from the free energy vs. polarization curves for first- and second-order transitions as shown in Figures 2.8 a) and b). Devonshire[32] has shown that the free energy of a ferroelectric under zero stress can be expressed as the

Taylor expansion,

$$G = \frac{1}{2}\chi P^2 + \frac{1}{4}\xi P^4 + \frac{1}{6}\zeta P^6 + \dots , \qquad [2.8]$$

where the coefficients χ, ξ and ζ are functions of the temperature. Devonshire further showed that with the application of a D.C. bias (electric field) the transition blurs and the polarization vs. temperature curve is no longer discontinuous for a second-order transition, as shown in Figures 2.7 a) and b).

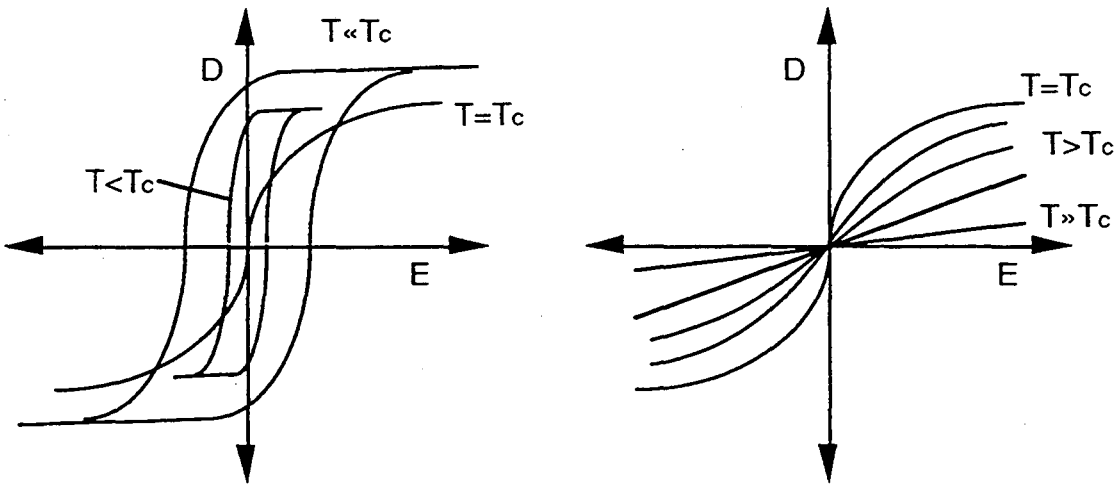

a) Ferroelectric Phase b) Paraelectric Phase

2.9. Electric displacement (D) vs. electric field (E) of a ferroelectric.

The behavior of the electric displacement (total polarization) vs. electric field as a function of temperature is important when considering ferroelectric materials for use as bolometers. The ferroelectric phase exhibits a hysteresis loop that changes with temperature, as illustrated in Figure 2.9 a). Figure 2.9 b) shows that near the Curie temperature in the paraelectric phase ($T > T_C$) the ferroelectric behaves as a non-linear dielectric. Far above the Curie temperature the ferroelectric behaves as a linear dielectric. Plotting these dependencies in three dimensions and taking two-dimensional cuts results in the displacement vs. temperature curves demonstrated in Figures 2.7 a) and b).

3. PYROELECTRIC DETECTORS

3.1 Pyroelectric Current

Pyroelectric detectors are bolometers that use the temperature dependent pyroelectric effect to detect incident radiation. The pyroelectric effect is represented by the pyroelectric coefficient vector. The pyroelectric coefficient (**p**) is the rate of change of the electric displacement (**D**), or polarization (**P**), of a pyroelectric material with temperature,

$$\mathbf{p} = \frac{d\mathbf{D}}{dT}. \qquad [3.1]$$

In a pyroelectric material where the dielectric constant is sensitive to finite temperature changes, as in a ferroelectric near the Curie temperature, Eq. [3.1] combined with Eq. [2.6] becomes

$$\mathbf{p} = \left[\frac{d\varepsilon}{dT}\right]_E \varepsilon_o \mathbf{E} + \left[\frac{d\mathbf{P}_s}{dT}\right]_E. \qquad [3.2]$$

In the absence of a D.C. bias, the first term in Eq. [3.2] is zero and the value of the pyroelectric coefficient depends only on the spontaneous polarization.

When electrodes† are applied to a pyroelectric material, as shown in Figure 3.1, changes in temperature produce charge flow between the electrodes; the resulting current is the pyroelectric current,

$$i_p = Ap\frac{dT}{dt}. \qquad [3.3]$$

Since the pyroelectric current depends on the temperature change with time, pyroelectric devices are considered to be 'AC coupled' to any temperature changing effect.[33]

† The electrodes are oriented normal to the polar axis of the pyroelectric.

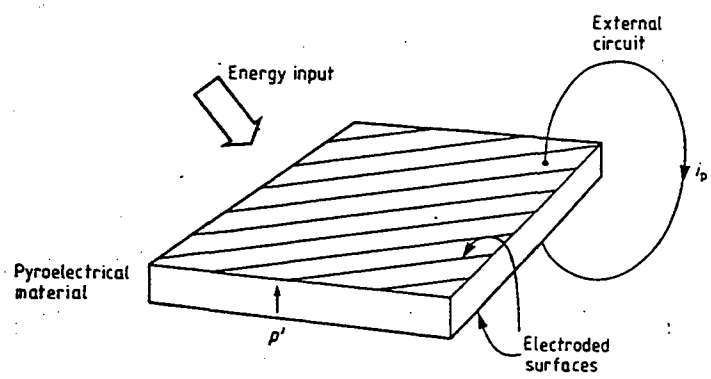

Figure 3.1. Electroded pyroelectric element showing flow of pyroelectric current due to a change in temperature (from Ref. 33).

3.2 Responsivity

Determining the electrical response of a pyroelectric detector requires analysis of both the thermal and electrical circuits. Measurement of the electrical response is usually made using the detector arrangement shown in Figure 3.2.[34] The detector is a thin plate of pyroelectric material contacted with electrodes normal to a polar axis. The simplest arrangement is to suspend the detector element in a vacuum by its wire leads. The wire leads carry charge to and from the electrodes and can be used to control the thermal conductance (G) between the element and its environment.

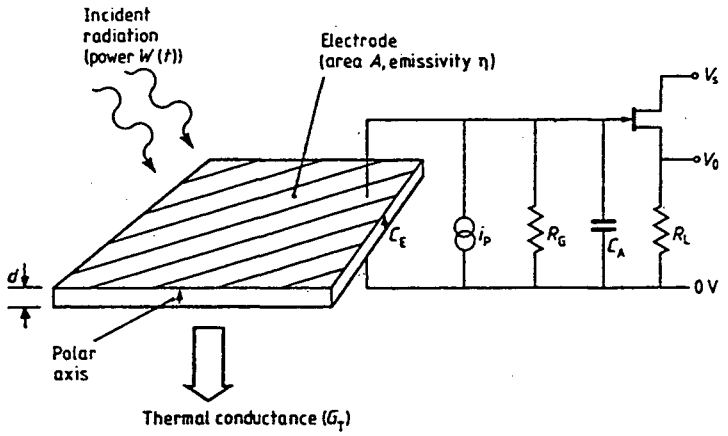

Figure 3.2. Schematic of a pyroelectric radiation detector and external circuit (from Ref. 34).

A pyroelectric detector is typically exposed to a sinusoidally modulated beam of radiation with power,

$$P = P_0 (1 + e^{i\omega t}) \qquad [3.4]$$

at an angular frequency, ω. Thermal sources usually produce continuous radiation. It is necessary to modulate the incoming radiation to obtain a thermal gradient, which produces the pyroelectric current (Eq. [3.3]). Typically, modulation of the radiation is achieved by mechanical chopping with a rotating disc.[35]

Absorption of the incident radiation results in a temperature rise (θ) of the sensor. The thermal response of the sensor to this change in temperature is dependent on the heat capacity (H) of the detector and the thermal conductance (G) coupling the detector to its surroundings. The combined effect of these factors is described by the equation for a thermal circuit,[36]

$$\eta P = H\frac{d\theta}{dt} + G\theta . \qquad [3.5]$$

Solving Eq. [3.5] for the sinusoidal power fluctuations given in equation [3.4] results in a temperature fluctuation amplitude θ_ω of the detector,

$$\theta_\omega = \eta P_\omega \left(G^2 + \omega^2 H^2\right)^{-1/2}. \qquad [3.6]$$

The phase difference between the incident radiation and the temperature oscillations is given by

$$\phi = \tan^{-1}\left(\omega H/G\right), \qquad [3.7]$$

and the thermal time constant is

$$\tau_T = \frac{H}{G} = \frac{cAd}{G}. \qquad [3.8]$$

The specific heat of the detector material and the area and thickness of the detector are c, A and d, respectively.

The thermal conductance between the detector element and its surroundings is determined by its radiative conductance (G_R) and the thermal conductance of the wire links (G_W).

$$G = G_R + G_W \qquad [3.9]$$

The radiative conductance is given by the Stefan-Boltzmann Law of thermal radiation,

$$G_R = 4\eta\sigma T^3 A_R, \qquad [3.10]$$

where σ is the Stefan-Boltzmann constant and A_R is the radiating area with emissivity, η. The thermal conductance through a wire is

$$G_W = \frac{\kappa A_W}{l} \qquad [3.11]$$

where κ is the thermal conductivity, A_W is the cross-sectional area and l is the length of the wire.[37]

The current responsivity[38] is defined as the current per watt of incident power,

$$R_i = \frac{i_p}{P_o}. \qquad [3.12]$$

Inserting equations [3.3] and [3.8] into equation [3.6] and rearranging results in

$$R_i = \frac{\eta \mathbf{p} A \omega}{G\left(1+\omega^2\tau_T^2\right)^{1/2}}. \qquad [3.13]$$

To determine the voltage response of the device the electrical circuit of Figure 3.2 must be considered. The voltage response of the detector,

$$R_V = \frac{V}{P_o} = \frac{i_p |Z|}{P_o}, \qquad [3.14]$$

depends on the electrical impedance of the circuit,

$$|Z| = \frac{R}{\left(1+\omega^2\tau_E^2\right)^{1/2}}, \qquad [3.14]$$

where τ_E=RC is the electrical time constant. The total circuit capacitance and resistance are, respectively, $C = C_E + C_A$ and $R = 1/(1/R_E + 1/R_G + 1/R_L)$, see Figure 3.2. Combining equations [3.12], [3.13], [3.14] and [3.15] results in the following voltage response:

$$R_V = \frac{\eta \mathbf{p} A \omega R}{G\left(1+\omega^2\tau_T^2\right)^{1/2}\left(1+\omega^2\tau_E^2\right)^{1/2}}. \qquad [3.16]$$

To achieve the greatest voltage response the impedance of the detector-load circuit and the current response must be maximized. The impedance is maximized with large R, and small ω and C The current response, Eq. [3.13], is maximized with large η and **p**, and small c and d.

The chopping frequency can have a significant effect on the magnitude of the voltage response of the detector. Figure 3.3 shows the dependence of the voltage response on the chopping frequency ($f=\omega/2\pi$). This curve depends on the properties of the different materials and the choice of τ_E. The sloped regions of the curve are referred to as the electrical and thermal roll-offs,

respectively, for the case shown. In the low frequency regime, Eq. [3.16] simplifies to

$$R_V = \frac{\eta p A \omega R}{G}. \qquad [3.17]$$

For medium frequencies Eq. [3.15] reduces to

$$R_V = \frac{\eta p R}{cd\left(1+\omega^2\tau_E^2\right)^{1/2}}. \qquad [3.18]$$

At high frequencies Eq. [3.15] is

$$R_V = \frac{\eta p}{cd\omega C}. \qquad [3.19]$$

The three preceding equations describe the dependence of the voltage responsivity on the thermal and electrical circuits, as well as on the materials properties and detector parameters. For example, if the capacitance of the detector is significantly greater than that of the amplifier, $C_E >> C_A$, then the responsivity in the high frequency regime is completely dependent on the emissivity, pyroelectric coefficient, specific heat, detector area and the dielectric permittivity of the detector. Altering one of these parameters shifts the high-frequency response to lower or higher frequencies.

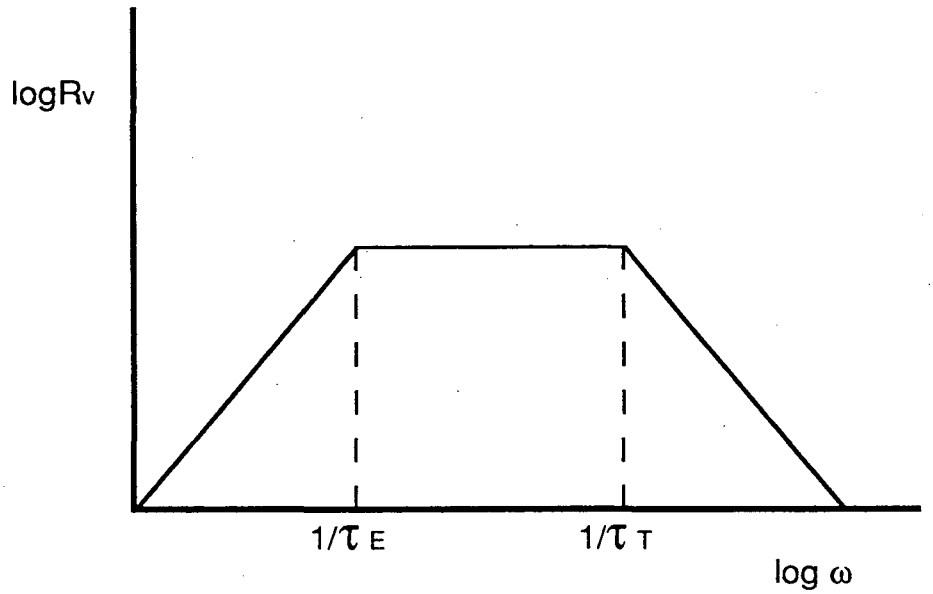

Figure 3.3. Schematic log-log plot of the Voltage Responsivity vs. Chopping Frequency.

3.3 Noise

To determine the detector performance it is insufficient to consider only its response. The minimum detectable signal is limited by various noise sources in the detector element and in the load and measuring circuit.[39] The sensitivity of a bolometric element is often expressed as the noise equivalent power (NEP). The NEP is the signal power incident on the bolometer which produces a signal-to-noise ratio of unity per 1 Hz electronic band width,

$$NEP = \frac{\Delta V_N}{R_V}. \qquad [3.20]$$

The detectivity is defined as the inverse of the NEP,

$$D = \frac{1}{NEP}, \qquad [3.21]$$

and the specific detectivity is $D^* = A^{1/2} D$. The use of D^* in the discussion of the performance of pyroelectric detectors can be misleading because some of the noise sources depend on the area (A) of the detector.[40]

The primary electronic noise sources for the circuit in Figure 3.2 are the temperature or radiation noise, Johnson noise of the equivalent circuit and amplifier current and voltage noise. The sum of the square of these noise terms is the total noise power squared,

$$\Delta V_N^2 = \Delta V_T^2 + \Delta V_J^2 + \Delta V_I^2 + \Delta V_A^2. \qquad [3.22]$$

Each term in Eq. [3.22] depends on frequency and refers to unit bandwidth.

Thermal noise is the change in output voltage that arises from random changes in the temperature of the pyroelectric detector. These thermal fluctuations are produced by the random exchange of heat and photons between the detector and its surroundings. For a detector linked to its surroundings by wire leads and situated in an evacuated chamber, the thermal noise arises from the thermal radiation, G_r, impinging on the detector and the thermal conductance, G_w, of the wire leads. The thermal noise voltage is

$$\Delta V_T = \frac{R_V}{\eta}\left(4kT^2G\right)^{1/2} \qquad [3.23]$$

where $G = G_r + G_w$. To minimize the thermal noise it is necessary to minimize the thermal conductance and the operation temperature. The smallest value of the thermal noise for a given temperature is obtained when the radiative conductance dominates the thermal conductance.[41] The ultimate detector sensitivity is limited by background radiation fluctuations. The thermal noise of a radiation limited detector depends on the temperature as $T^{5/2}$.

Johnson noise arises from the random motion of charge carriers in the crystal and in the electrical circuit. In practice, the pyroelectric crystal is not a perfect capacitor; the dielectric loss of the crystal is one factor contributing to the detector Johnson noise.[42] The Johnson noise voltage per unit bandwidth[43] is given by

$$\Delta V_J = \left(\frac{4kT}{R}\right)^{1/2}\left(\frac{1}{R^2} + \omega^2 C^2\right)^{-1/2}. \qquad [3.24]$$

The total resistance, R, is the parallel value of the gate resistance, R_G, and loss equivalent resistance, $R_E = (\omega C_E \tan\delta)^{-1}$. Likewise, C is the total capacitance of the detector, C_E, and circuit, C_A, in parallel.[44] At low frequencies, $\omega \ll (R_G C_E \tan\delta)^{-1}$, Eq. [3.24] simplifies to

$$\Delta V_J = \left(\frac{4kTR_G}{1 + \frac{1}{\tan^2\delta}}\right)^{1/2} \qquad C_E \gg C_A. \qquad [3.25]$$

In the preceding equation the Johnson noise is minimized by low temperature operation, and small R_G and dielectric loss, $\tan\delta$ (Eq. [2.2]). The high frequency approximation, $\omega \gg (R_G C_E \tan\delta)^{-1}$, simplifies the Johnson noise voltage to

$$\Delta V_J = \left(4kT\frac{\tan\delta}{\omega C_E}\right)^{1/2} \qquad C_E \gg C_A. \qquad [3.26]$$

Minimizing the Johnson noise† in high-frequency operation is accomplished by operating at low temperature and high frequency with a large detector capacitance.

Other noise sources are the electrical equipment, such as the signal amplifier, and microphonic effects.[45] The signal amplifier noise depends on the gate leakage current of the FET and the preamplifier voltage noise. It is represented as a current generator or voltage in parallel with the input circuit.[46] Microphonic noise is caused by vibrations of the electrical components. Vibration in the wire leads may result in charge fluctuations (dQ = VdC + CdV) and/or capacitance changes. In addition, since pyroelectric materials are also piezoelectric, vibrations can create stresses causing fluctuations in the

† The capacitance (dielectric constant) and dielectric loss are frequency dependent in ferroelectrics.[43]

spontaneous polarization (pyroelectric coefficient). These changes in the electrical behavior of the circuit may be significant and produce currents that are not due to the signal being measured.[47]

3.4 Radiation Absorption

The bolometer response is increased by maximizing the incident radiation absorption in the wavelength range of interest by the device or a thermally connected antenna. Since the bolometer's noise response depends on its heat capacity, any radiation coupling method must not raise the heat capacity and/or the thermal time constant of the element significantly. Methods used to increase the absorption or emissivity include impedance matching, absorbing films and transparent electrodes. Separating the functions of radiation absorption and measurement of temperature fluctuations of a bolometer has led to the composite detector.

Impedance matching is typically achieved by adjusting the thickness of a metal layer such as bismuth or NiCr on a dielectric substrate to match its impedance to free space. Maximum absorption occurs when the surrounding impedance, for this application the impedance of a vacuum, matches the metal film impedance modified by the dielectric substrates index of refraction. Typically, the detector material is not used as the dielectric substrate but is thermally attached to the bolometer resulting in a composite bolometer. However, in the case of pyroelectric detectors the detector material may be used as the dielectric substrate.

Application of an absorbing layer to the bolometer is conceptually the simplest method used to increase the absorption of detectors. Carbon black, gold black, platinum black, and black paint are all potential choices for an absorbing layer. Carbon black is naturally black over a range of wavelengths

that depends on the size of carbon particles. Gold and platinum black are produced by creating porous films of sputtered gold or platinum. Black paint incorporates carbon black or other blackening agents in a suspension that is applied in liquid form.

The use of a transparent front electrode is ideal for detector materials that absorb in the wavelength of interest.[48] Single crystal pyroelectric materials typically have strong absorption from about 10μm to submillimeter wavelengths and are relatively transparent in the visible and UV wavelengths.[49] Reducing the thickness of applied metal electrodes allows greater radiation transmission. In semiconductor devices sometimes one of the metal contacts is omitted allowing passage of the radiation. The device contact is then provided by a heavily implanted layer at the surface.

The composite bolometer is used often for semiconductor bolometers. The functions of absorbing and measuring the rise in temperature are accomplished by two thermally attached materials. Radiation absorption is increased by impedance matching a highly resistive metal and a low specific heat material, such as sapphire or pure silicon, with the surroundings. The detector is then thermally connected to this absorber.

4. MATERIALS

4.1 Properties and Selection Criteria

Chapter 3 describes how the detector response and noise sources depend on the materials properties. The most important property for pyroelectric detection is the pyroelectric coefficient. Since the highest pyroelectric coefficients are observed in the ferroelectric materials, it is desirable to choose from the class of ferroelectric materials for fabrication of pyroelectric detectors. Ferroelectric materials have the highest values of the pyroelectric coefficient near their Curie temperature. Therefore, it is preferred that the Curie temperature of the ferroelectric material lie near the intended detector operating temperature. To achieve the best performance for the requirements given in Chapter 1 these detectors are designed to operate near 100K.

Table 4.1. Transition temperatures of ferroelectrics of the KDP family

Material	Formula	T_c (K)
KDA	KH_2SO_4	96
RDA	RbH_2SO_4	110
KDP	KH_2PO_4	123
CDA	CsH_2AsO_4	143
ADP	$NH_4H_2PO_4$	147
RDP	RbH_2PO_4	147

Ferroelectric materials that have a Curie temperature in the proximity of 100K are members of the KDP (Table 4.1,[50]) and KTN families. The Curie temperature of KTN can be adjusted to any given temperature between 0-705K by alloying.[51] Detectors have been fabricated from KDP and KTN. KDP was chosen from the KDP family because of its availability as pure, large crystals;

although, KDA has the largest pyroelectric coefficient. The KDP crystals are provided by Jeff Atherton and Eberhard Prochnow of the Advanced Lasers Group at Lawrence Livermore National Laboratory. The KTN crystals are obtained from Dr. Daniel Rytz of the Optoelectronics Division, Sandoz Corporation, France.

4.2 Potassium Dihydrogen Phosphate (KDP)

The structure of KH_2PO_4 consists of two interpenetrating body-centered K lattices intertwined with a lattice of PO_4 tetrahedra, as shown in Figure 4.1. Each potassium ion is surrounded by eight oxygen atoms that belong to the PO_4 groups. Every PO_4 group is linked to four other PO_4 groups by hydrogen bonds that are almost perpendicular to the c-axis (ferroelectric axis). Each hydrogen bond links one upper oxygen of one PO_4 group to a lower oxygen of a neighboring group. Only two hydrogen atoms are normally located near any one PO_4 giving rise to the formal ionic configuration $K^+(H_2PO_4)^-$.

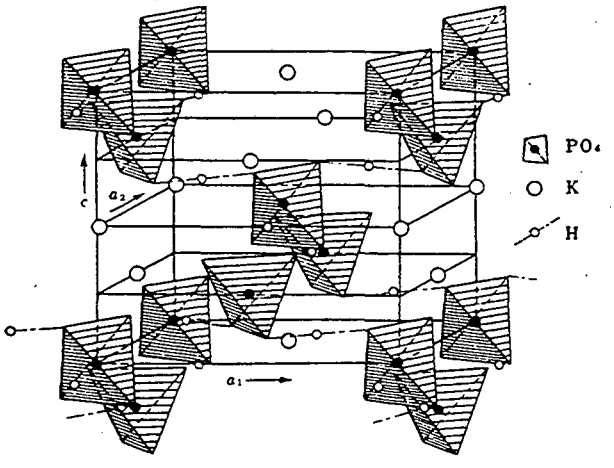

Figure 4.1. The crystal structure of KH_2PO_4 (from Ref. 52). .

The Curie transition in KDP is a sharp second-order transition.[52] The transition is triggered by an order–disorder transition of the protons in the O-H-··· O bonds. The motion of the protons along the hydrogen bonds is strongly coupled to displacements of the other ions along the c-axis. In the paraelectric phase the protons are statistically distributed between the two PO_4 groups along the H-bond. In the ferroelectric phase, however, protons order near one of the two PO_4 groups. In a single domain all hydrogen atoms order like their neighbors giving rise to the spontaneous electric moment.[53,54,55]

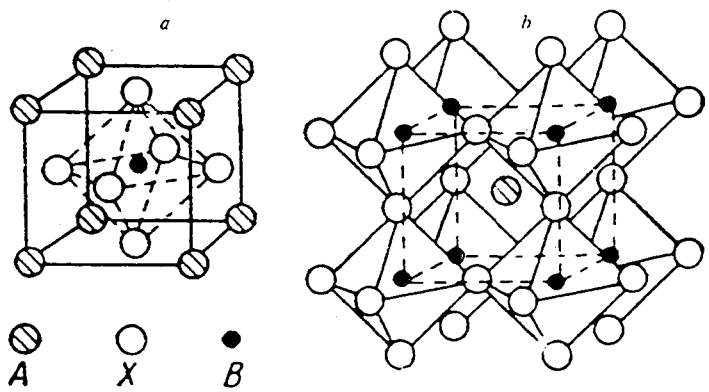

Figure 4.2. Perovskite-type crystal structure: (a) Unit cell (b) The structural framework consisting of octahedra (from Ref. 57).

4.3 Potassium Tantalate Niobate (KTN)

KTN belongs to the perovskite group of ferroelectrics. Crystals with the perovskite structure have a general chemical formula, ABX_3; A and B are cations and X is the oxygen anion. The prototype structure is cubic and has BX_6 oxygen octahedra linked in a cubic lattice, as illustrated in Figure 4.2. Polarization in these perovskites arises from displacements of the A-cations.

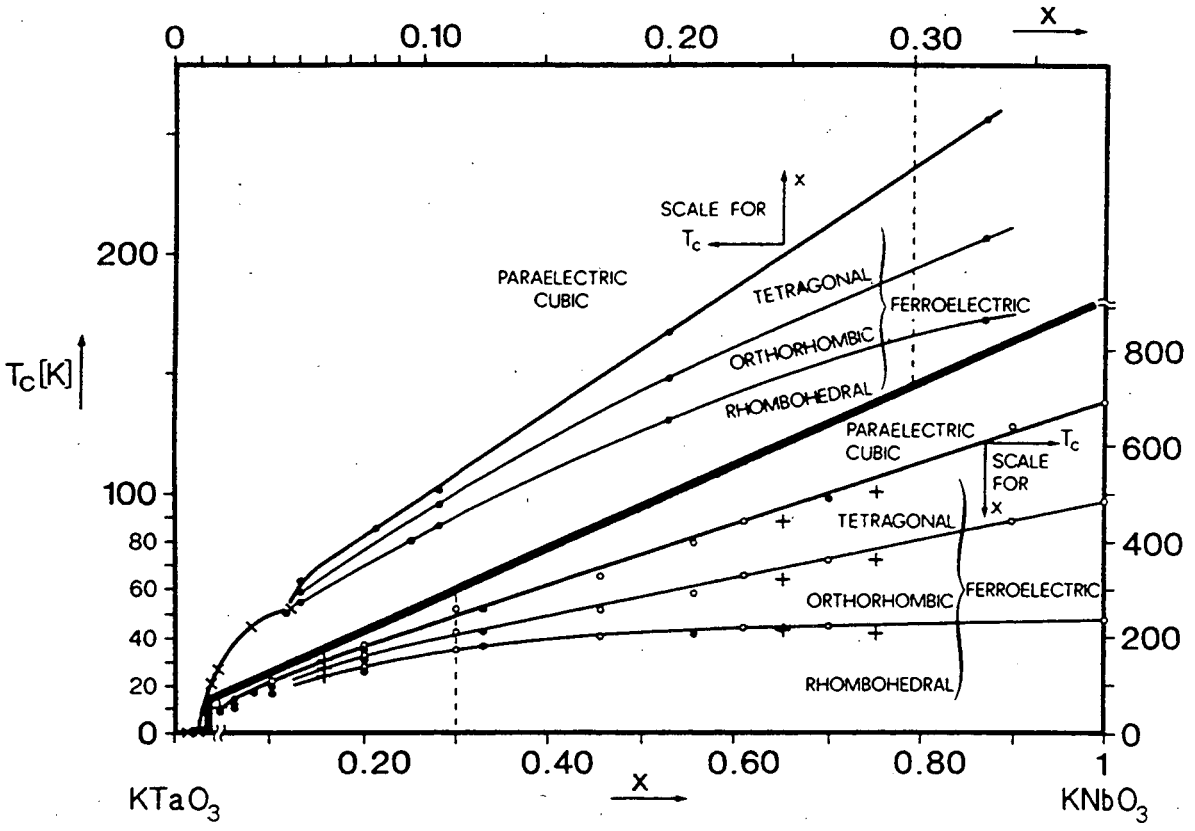

Figure 4.3. Phase transitions of KTN as a function of tantalate fraction, x (from Ref. 58).

In KTN ($KTa_xNb_{1-x}O_3$) the body centered positions, B, are shared by Ta and Nb. The Curie temperature and the temperature of the ferroelectric-ferroelectric transitions vary linearly with composition,[58] as shown in Figure 4.3. The Curie temperature is determined with the empirical equation:

$$T_c = 676\,x + 32 \qquad (K) \qquad [4.1]$$

when $x \geq 0.047$. For a tantalate fraction, $x > 0.30$, the Curie transition is first order and for $x < 0.30$ it is second order.[58] The spontaneous polarization of tetragonal KTN results in 90° domains. During the cubic to tetragonal transition the distortion of the lattice and thus the direction of the tetragonal c-axis can occur along any three of the identical cubic axis. Therefore, polarization exists along any of these three orthogonal axes leading to 90° domains.[56,57]

5. SAMPLE PREPARATION

5.1 KDP

Several new processing techniques were devised for making thin capacitative samples of KDP. The material has low mechanical integrity, is soluble in water, and tends to decompose when heated above 120°C. This combination of physical properties makes thin device fabrication a challenge. The general processing steps are as follows: (1) cut sample from bulk crystal, (2) polish sample to device thickness, (3) metallize sample, and (4) cut sample into device sizes. The most successful processing methods are as follows:

First the bulk crystal is oriented, and the direction of the c-axis (polar) is noted so that samples can be cut with the c-axis perpendicular to the plane of the intended contacts. Orientation of the KDP is accomplished by using the transparent and anisotropic nature of the material. At room temperature KDP has a tetragonal crystal structure therefore the bond strength within the (001) plane is different than between these planes. Light transmitted through the crystal along the c-axis experiences no preferred vibration direction. Light traveling at some angle to the c-axis will experience two different vibration directions, splitting the light into two rays with different velocities. This behavior results in an interference pattern when observing the cross-polarized light transmitted through the crystal,[59] as shown in Figure 5.1. When the c-axis is perpendicular to the crossed-polarizers the interference pattern does not move or change as the crystal is rotated in the plane of the polarizers.

After orientation, the crystal is mounted on a graphite block with the c-axis parallel to the block. Paraffin wax (melting temperature 52°C) is used as the adhesive. KDP can crack when subjected to small thermal gradients; so,

great care is taken to heat and cool the samples uniformly. The bulk KDP is cut into slabs 0.3-1mm thick with a high-concentration diamond wafering blade using isocut oil†. After cutting, the wafer is removed from the cutting block and immersed in TCA to remove surface residues. The cleaned wafer is then waxed to a polishing fixture.

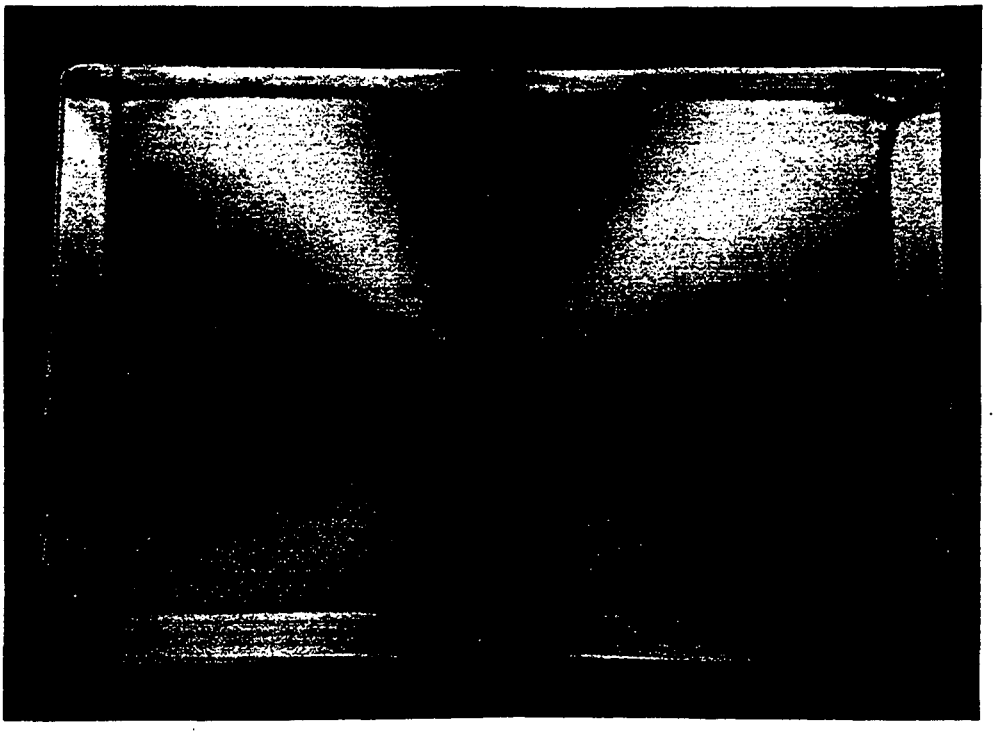

Figure 5.1. Interference pattern for a KDP crystal with light traveling parallel to the optic axis (c-axis). The point where the to black bars cross marks the emergence of the optic axis. The circular bands are interference colors which increase in order outward from the center of the cross.

† Most cutting devices are unsuitable for use with KDP because they use water; KDP is water soluble.

The surfaces are mechanically polished using a mixture of 0.3μm aluminum oxide and ethylene glycol. After one side is polished, the polished surface is rinsed with ethylene glycol and xylene. TCA cannot be used on the polished KDP surface because it contains enough water to preferentially etch the surface. The sample is then blown dry with nitrogen gas and remounted on a water-cooled plate without disturbing the polished surface. Polishing one face of the KDP sample and then immediately metallizing it preserves the optically smooth surface, helps ground the small sample reducing the electrostatic effect when handling, and adds strength, making the polishing of thin samples possible. The polished side of the sample is now ready for metallization. The water-cooled plate is mounted inside an RF-driven sputtering machine and, typically, 200Å of palladium followed immediately by 1400Å of gold are deposited onto the polished surface. Palladium acts as a wetting and adhesion layer. Gold provides chemical inertness and good electrical conduction. Following metallization, the opposite unmetallized surface is polished until the final desired device thickness is attained. This surface is then sputter coated as discussed above. Small test samples are cut from the prepared crystal using a wire saw with an ethylene glycol/alumina slurry cutting agent. No slurry is used when cutting very thin samples (<100μm).

Although devices have been produced using the preceding steps, the process has a rather low yield and the resulting contacts are not very rugged and durable. Several hypotheses were put forth to explain the failure of the contacts: (1) difference in thermal expansion between the substrate and the contact metal, (2) poor bonding between the KDP and the wetting metal, and (3) a dirty KDP surface prior to metal deposition.

First, failure due to differences in thermal expansion was dismissed because other electronic devices processed in our lab with greater differences

in thermal expansion with their metal contacts do not show contact failure. Second, several different wetting metals were tried, unsuccessfully, in an attempt to promote wetting between the KDP and the contacts. Cr was one of the wetting metals tried and it is known to be very reactive. The picture in Figure 5.2 is an example of a failed Pd:Au contact on KDP taken through a microscope. The contact shows a wrinkled morphology intermixed with raised jagged lines. This morphology suggests that raised lines initiated as small formations that subsequently propagated across the contact. Since there is no difficulty in adhesion of various wetting metals with SiO_2, a SiO_2 layer was also attempted to promote wetting with the KDP. The SiO_2 was sputtered on before deposition of a Pd:Au contact. Figure 5.3 is a picture of the failed contact. The morphology of this raised "bubble-like" surface is not unique to samples with an SiO_2 wetting layer. Lastly, to remove particulates on the surface an in situ clean was attempted by sputter etching the samples prior to deposition of the metal films. Because the samples were so thin, metal from the mounting plate sputtered up and onto the surface making this process unsuccessful.

Typically, failure of the contacts did not occur until processing of the sample after metallization. Directly after depositing the metal contacts the adhesion appears to be good. It wasn't until the subsequent processing steps that the contacts started to degrade. Heating contributes to the contact degradation; the water solubility of the KDP increases upon heating and upon cooling the excess water vaporizes from the KDP lifting off the contacts. In addition, the bonding is weakened by cleaning, exposure to air (humidity), and cutting of test samples. The cause of the poor adhesion of the metal contacts was decided to be due, primarily, to the hygroscopic nature of the KDP.

The successful preparation of KDP devices requires a minimum in processing. Care must be taken to not excessively heat or expose the metallized surfaces to water.

5.2 KTN

By comparison with KDP, the process used to fabricate KTN bolometers is relatively straightforward; KTN is hard and ceramic-like and, thus, more tolerant of handling than the KDP. The KTN sample is lapped using 9μm followed by 3μm Al_2O_3 grit. A polyurethane polishing pad with syton solution is used to polish the KTN until an optically smooth surface is obtained. The polished sample is cleaned using separate rinses of TCA, methanol, acetone and finally water. Next, the sample is loaded into the sputtering machine where 200-250Å of chromium followed (immediately) by 1400Å of gold, without breaking the vacuum, are RF-sputtered onto the polished surface. Then the opposite side of the sample undergoes the polishing and sputtering process. The metallized KTN wafer is then cut into small devices using a dicing saw.

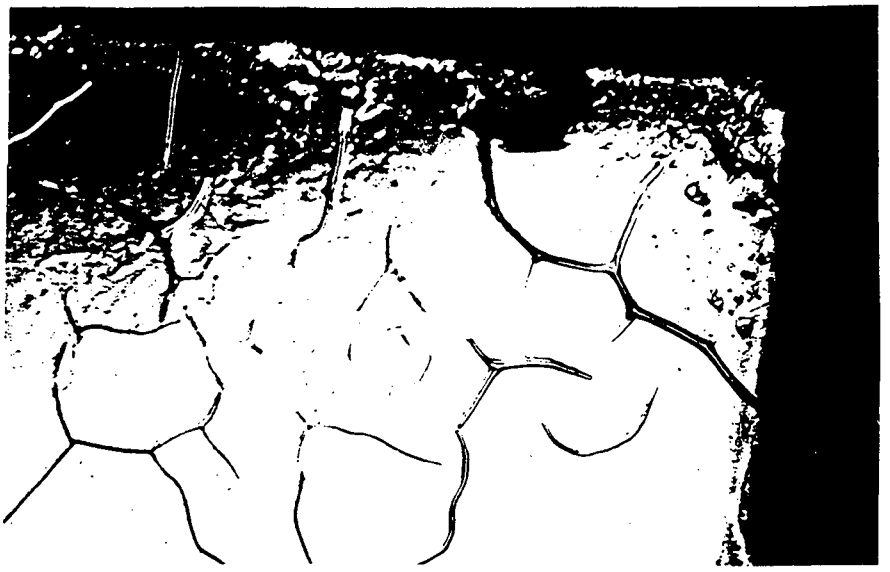

Figure 5.2. Surface of a KDP sample with sputter deposited layers of Pd (200Å) followed by Au (1400Å). Magnification - 80x. The wrinkled surface appeared during heating in TCA to remove wax.

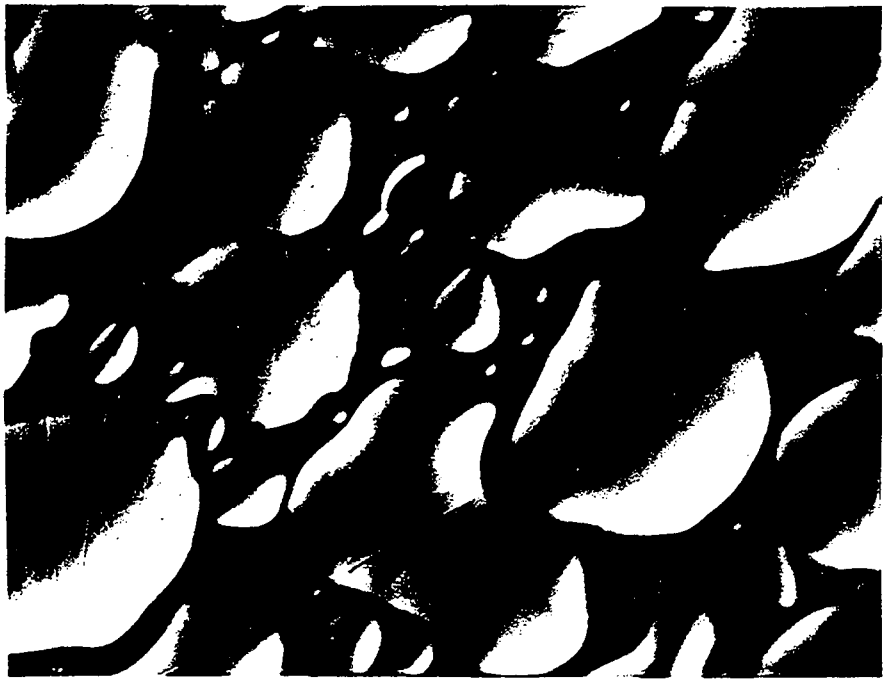

Figure 5.3. Surface of a KDP sample with sputter deposited layers of SiO_2 (190Å) followed by Pd (200Å) and Au (1400Å). Magnification - 600x. The bubbled morphology appeared immediately after removing from the sputtering machine.

6.0 DETECTOR CONFIGURATION

6.1 Detector Mount

In order to measure the response of the pyroelectric device it must be connected to the electrical circuit while simultaneously situated to absorb incoming radiation. The detectors characterized in this thesis are supported solely by the electrical wires, which are connected to the electrical circuit through a supporting mounting plate.

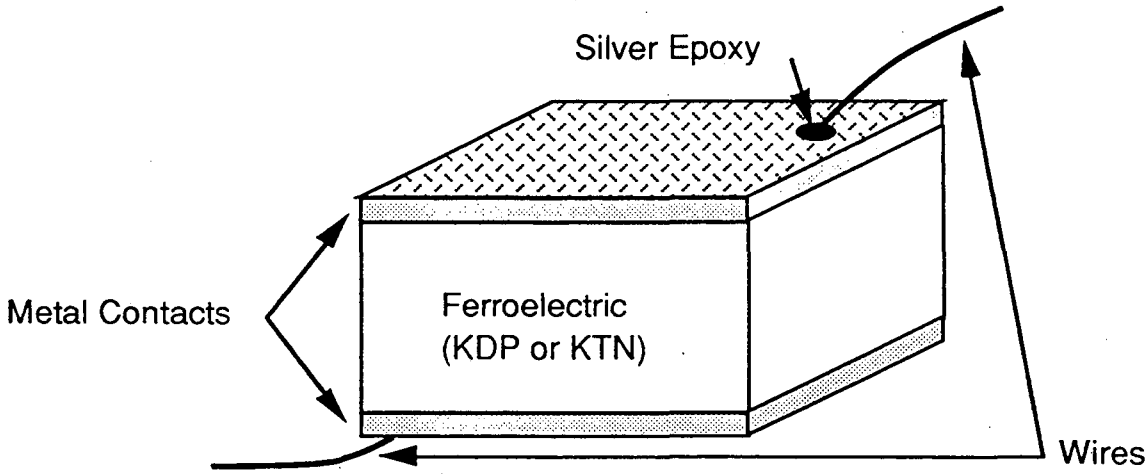

Figure 6.1. Pyroelectric device with attached wires for connection to electrical circuit. Dimensions: KDP - 0.25mm^2 x 25μm and KTN - 1mm^2 x 60μm. Metal Contacts: KDP - Pd:Au 200:1400Å and KTN - Cr:Au 200:1400Å. Note that the contacts are drawn disproportionately thick.

The detector processing described in Sections 5.1 and 5.2 for KDP and KTN, respectively, result in thin capacitative devices, see Figure 6.1. Electrical wires are attached to the electrodes of these devices using a conducting silver epoxy†. Curing is performed at 80°C for 90 minutes with KDP and at 120°C for 15 minutes with KTN. Wire leads can not be soldered to the metallized surface

† EPO-TEK H20E.

of the device itself due to its size and, in the case of KDP, its temperature sensitivity.

The configuration of the detector mounting arrangement greatly influences the performance of the pyroelectric detector. The mounting plate shown in Figure 6.2 is designed to allow control of the thermal conductance between the detector and the mounting plate by choosing the appropriate wire material, length and diameter. The mounting plate is a copper-coated G10 epoxy board. The horizontal lines drawn across the surface of the mounting plate indicate a separation between the copper surface above and below these lines. The copper has been cut through to the supporting epoxy board to form two electrically isolated copper contact pads. Electrical interconnects are soldered to these contact pads. The detector is supported by its electrical wires which are attached to the copper contact pads with the silver epoxy. The curing schedule is the same as that used to attach the wires to the device.

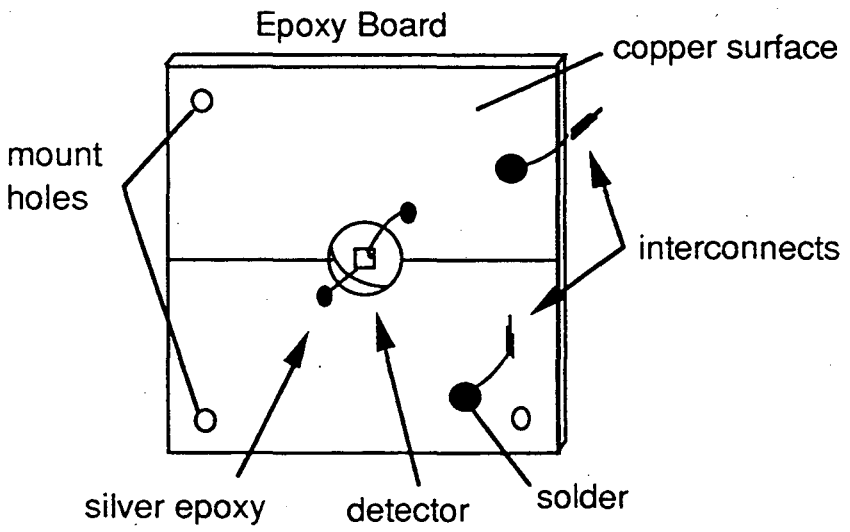

Figure 6.2. Detector mounting plate, top view.

6.2 Thermal Analysis

Theoretical thermal analysis is performed on a cooled KDP pyroelectric detector for comparison with commercially available pyroelectric detectors operating at room temperature. Once established that cooled pyroelectric detectors can exhibit enhanced performance over room temperature pyroelectric devices, the operating parameters of a cooled KDP device are investigated.

The performance of a thermal detector can be measured by its detectivity (Eq. [3.21]), as described in Section 3.3. Assuming that the noise is dominated by thermal fluctuations Equations [3.22] and [3.23] result in a detectivity,

$$D = \eta(4kT^2G)^{-1/2}, \qquad [6.1]$$

controlled by the thermal conductance, G, between the detector and its surroundings. To minimize the thermal conductance and, thus, maximize the detectivity, it is necessary to minimize the contributions to the thermal conductance from the wire leads and the thermal radiance of the detector, Eq. [3.9]. When the contribution from the wire leads is negligible, the thermal radiance, G_R, dominates and the detector detectivity is ultimately limited by the background temperature. Using Eq. [3.10] the detectivity of the background limited detector becomes

$$D = \eta^{1/2}(16k\sigma A_R T^5)^{-1/2}. \qquad [6.2]$$

Theoretical detectivity values for KDP are better than those of room temperature detectors currently in use. A room temperature TGS (triglycine sulphate) pyroelectric detector constructed at the Royal Radar Establishment has $D^* \sim 4.5\times10^7$ $cmHz^{-1/2}W^{-1}$ (with $A = 0.03$ $cm^2 \rightarrow D = 2.6\times10^8$ $cmHz^{-1/2}W^{-1}$)[60]; this is over three orders of magnitude worse than a theoretical KDP detector, $D = 4.2\times10^{11}$ $cmHz^{1/2}W^{-1}$, operating at 125K with an emissivity of $\eta = 0.2$. The variation of the detectivity with temperature for a detector with $A_R = 1mm^2$ is

shown in Figure 6.3 for emissivities equal to 1, 0.5, and 0.1. Reducing the detector operating temperature from 300K to 100K increases the background-limited device detectivity by over one order of magnitude. Additional increases in detectivity can be obtained by increasing the emissivity and/or reducing the area of the detector.

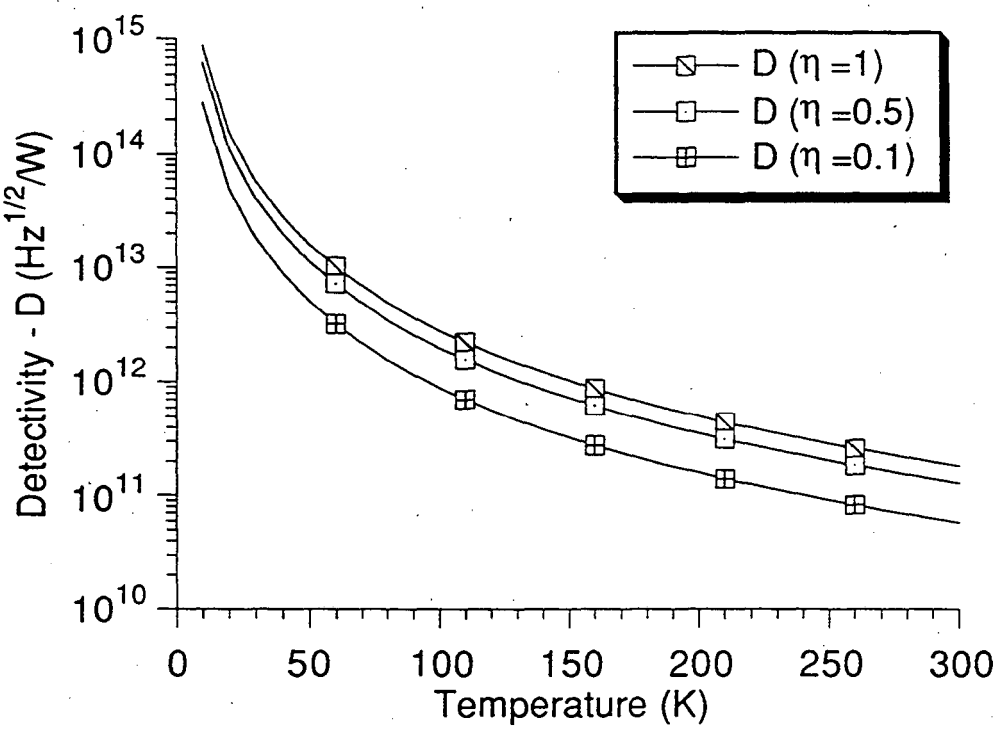

Figure 6.3. Background-limited detectivity vs. temperature for different emissivities assuming a 1mm^2 radiating area.

The intended operating temperature of these pyroelectric detectors is approximately 100K; this allows an increase in detectivity over detectors operating at room temperature while allowing the use of passive cooling (T > 85K). To construct a detector that is background limited at an operating temperature of 100K, the thermal conductance of the wire, G_W, attaching the

detector to its surroundings must be less then the thermal radiance, G_R, of the detector. A comparison between the thermal conductance of various wire types

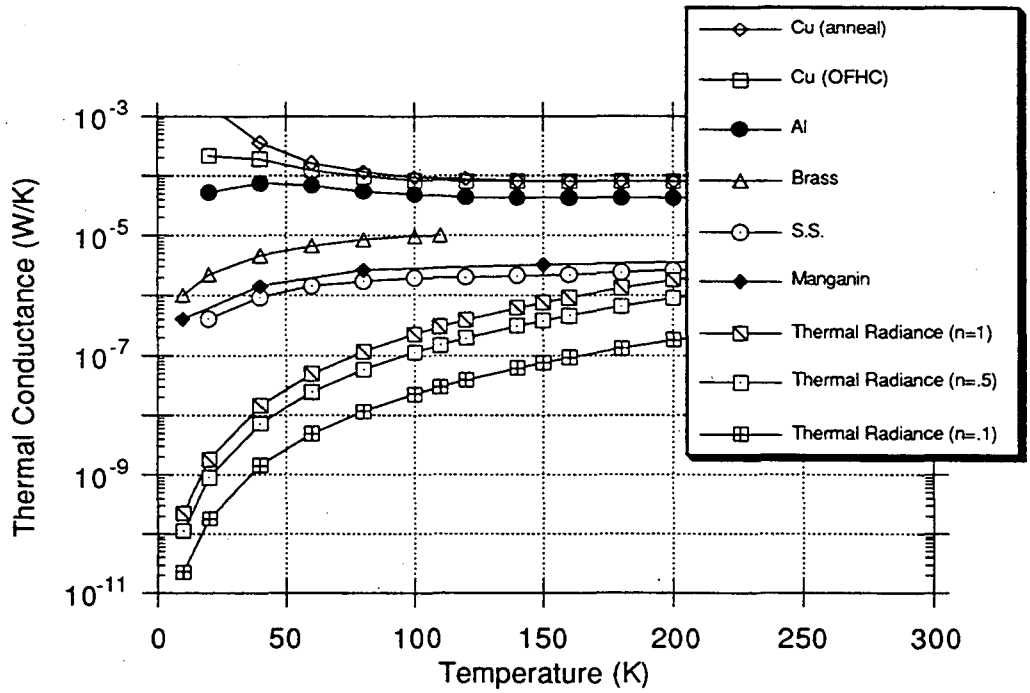

Figure 6.4. Thermal conductance vs. temperature for two 0.5 cm 1 mil metal wires and thermal radiance from a 1mm^2 radiating body.

and sizes and the thermal radiance of a detector is made to determine whether the background-limited case can be realized at 100K. Figures 6.4 and 6.5 show the thermal conductance vs. temperature of various 1 mil and 1/2 mil wires, respectively, compared with the thermal radiance vs. temperature of a 1mm^2 detector. The thermal radiance values were computed from Eq. [3.10] assuming a 1mm^2 body radiating from only one face with an emissivity of $\eta = 1$, $\eta = 0.5$, or $\eta = 0.1$. The thermal conductance values were computed using Eq. [3.11] for two 0.5cm long wires attached to the detector. Thermal conductivity vs. temperature data for the various metals were taken from the figure in Appendix B.[61,62] This analysis shows that by choosing an appropriate wire type and size (Ex. 1/2 mil manganin or S.S., Figure 6.5) it is possible to construct a

pyroelectric detector operating at 100K that is background limited; the thermal radiance term dominates the thermal conductance of the detector. The thermal radiance of the detector can be further reduced by decreasing the emissivity and radiating area. Both these approaches, however, lower the photon absorption in the detector and, therefore, may not increase the performance of the detector.

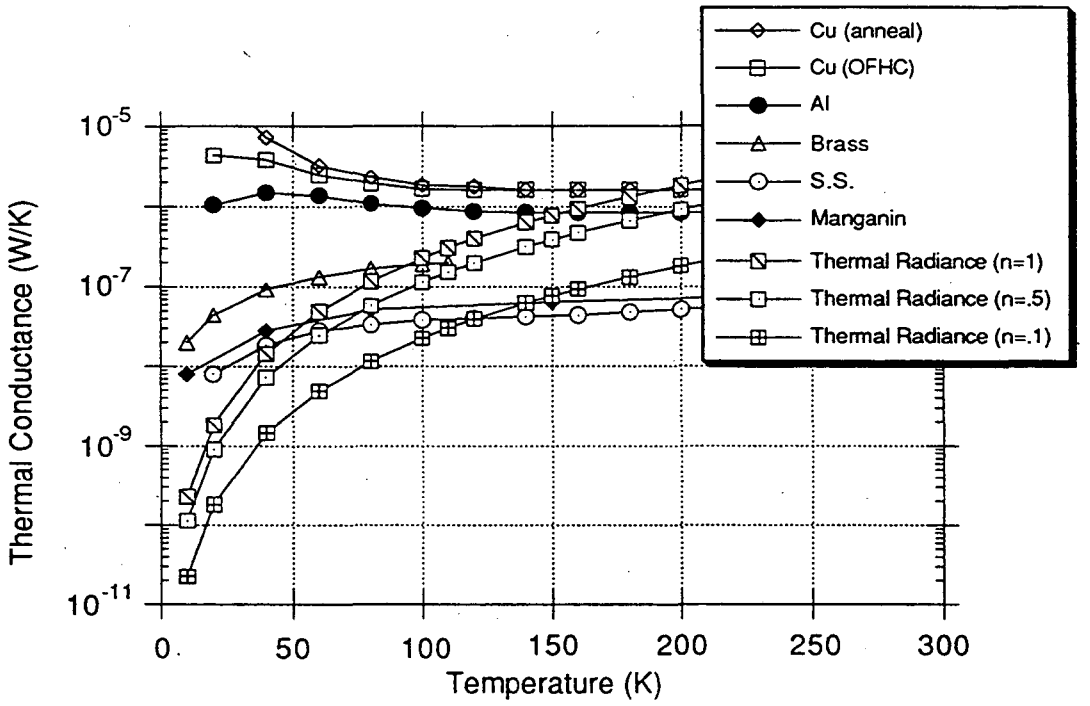

Figure 6.5. Thermal conductance vs. temperature for two 0.5cm 1/2 mil metal wires and thermal radiance from a 1mm^2 radiating body.

NASA's Earth Observing System requires that the detectors operate at a frequency of 10-20Hz. This frequency is dictated by the scanning speed of the telescope and the spatial resolution. Since pyroelectric detectors are A.C. coupled to the radiation source, the frequency is an important parameter to the design of the detector (Sections 3.1 and 3.2). The chopping frequency must be high enough to obtain a sampling frequency that allows resolving the time varying target image. The highest response and, therefore, the most desirable

operating region occurs in the medium frequency (flat response) range shown in Figure 3.3. The frequency at which the low frequency roll-off begins, in our case, depends on the electrical time constant, which is easily adjusted by choosing the appropriate coupling capacitor and resistor. The start of the high frequency roll-off is determined by the thermal time constant, which depends on the detector material, its size, and the thermal conductance between the detector and its surroundings. A background-limited KDP detector operating at 125K with the following realistic operating parameters:

C_p = 1.165 J/cm^{3}K (Appendix C)[63],

$A_r = A_d = 1 mm^2$,

d = 100μm,

and η = 0.2

has a radiative thermal conductance of $G_r = 8.86 \times 10^{-8}$ W/K resulting in a detectivity of 7.23×10^{11} Hz$^{1/2}$/W. Unfortunately, this also corresponds to a thermal time constant of $\tau = 1315$ s. The flat top responsivity rolls off at 1.2×10^{-4} Hz far below the minimum chopping frequency of 10-20 Hz.

To create the flat responsivity range at the detector operating frequency, f ~ 15Hz, it is necessary to choose the thermal, τ_T, and electrical, τ_E, time constants such that $\tau_T < 11ms < \tau_E$. Using Equations [3.8] and [6.1] with the above parameters, the thermal conductance and detectivity necessary for τ_T = 11ms for a KDP detector operating at T = 125K are $G = 1.06 \times 10^{-2}$ W/K and $D = 2.09 \times 10^9$ Hz$^{1/2}$/W. This results in a decrease in detectivity of over two orders of magnitude without an increase in the responsivity (Eq. [3.16]). Figure 6.6 exhibits the shift in responsivity vs. frequency keeping all detector parameters the same except the thermal conductance, which increases from its minimum value, G_R. Increasing the thermal conductance shifts the thermal time constant to higher frequencies while simultaneously decreasing the detectivity. At the

operating frequency shown, the responsivity remains constant until the thermal time constant corresponds to the operating frequency. Further increases in the thermal time constant reduce the responsivity. Since increasing the thermal conductance does not increase the responsivity but reduces the detectivity of the detector, it is better to operate these detectors on the high frequency roll-off portion of the responsivity curve to use the higher detectivity available at 125K. Eq. [3.19] describes the dependence of the high-frequency responsivity on various parameters and materials properties. The performance of the detector may change because of D.C. heating which can increase the temperature of the device beyond its optimum operating range. D.C. heating is due to the background radiation and the incoming signal. Since the incoming signal can carry significant power depending on its source, it is important to know the power of the radiation source being detected. The increase in temperature of the bolometric device by D.C. heating depends on the thermal conductance of the detector, G, and the incident D.C. radiation power, $P_{D.C.}$, on the device:

$$\Delta T = P_{D.C.}/G. \qquad [6.3]$$

A high-detectivity detector, $G = 10^{-7}$ W/K, will heat up 1 K for every 10^{-7} W of D.C. power.

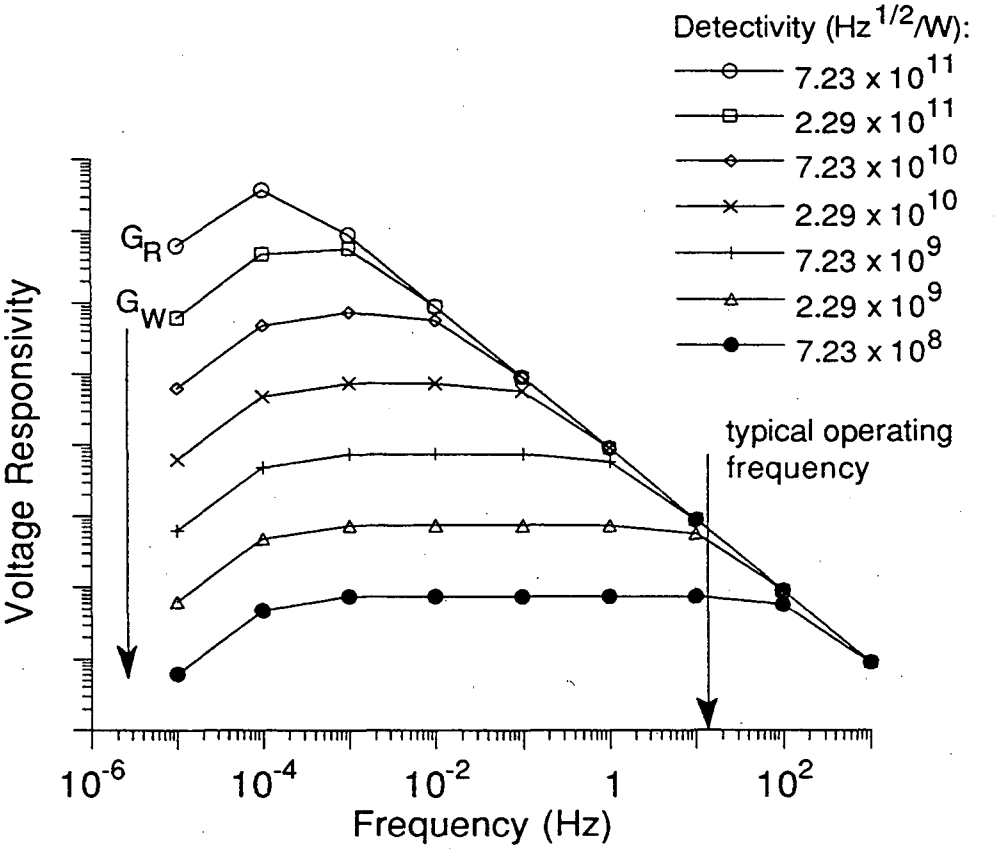

Figure 6.6. Responsivity vs. chopping frequency for a 1mm^2 x 100 μm KDP detector operating at 125K with an emissivity of $\eta = 0.2$

6.3 Absorbing Layer

The application of the absorbing layer is performed after wires have been attached to the device in Figure 6.1 to allow means to secure the tiny device. In addition, wires must be attached directly to the electrode surface to make a good electrical contact and this is not possible if the absorbing layer has already been applied.

The small size of the detectors makes it challenging to select a coating that has a sufficiently low heat capacity so that it does not significantly affect the thermal response characteristics of the device. Devices have been made using three types of absorbing layers. The first attempt was made with a xylene-

based "carbon black" liquid applied through a drawn capillary tube and evaporated. Two problems existed with this method. First, the solution was thin and tended to run over the sides of the detector causing an electrical short. Second, when the solution evaporated the carbon black coalesced leaving only part of the surface black. Another absorbing layer was made by spray painting Krylon Flat Black Paint through a pin hole onto a detector. Lining up the pin hole with the minuscule detector and controlling the thickness proved difficult. To eliminate these problems a thicker and more workable absorbing layer has been made. This black is made by mixing by weight a ratio of 6:1 of optically transparent epoxy† and carbon black††. The resulting mixture is more viscous and can be painted on the contact with a fine, soft brush-tip. In addition, once applied to the electrode surface it is still workable until cured. Curing is performed at 80°C for 90 minutes.

---

† EPO-TEK 301-2 optically transparent epoxy.
† † Carbon black R-5000 ultra powder - Columbia Chemicals Company.

7. ELECTRICAL CHARACTERIZATION

7.1 Capacitance Measurements

Measurements of a total of twelve KDP and KTN samples were made to determine their dielectric properties. Table 7.1 identifies the samples, sample sizes, contact metals and thicknesses. Measuring the capacitance and resistance and thus the dielectric permittivity and dielectric loss as a function of temperature gives three important results. First, it allows determination of the Curie temperature and the abruptness of the transition (see Chapter 2, Figure 2.6.). Second, the magnitude of the capacitance and dielectric loss of the ferroelectric material affect the responsivity of the detector (Chapter 3, Section 3.2). Third, the electrical time constant can be adjusted to give optimum frequency vs. response curves limiting the noise (Chapter 3, Section 3.3) to the detector and not its measuring circuit.

Determining the capacitance and loss of ferroelectric materials requires a measurement system with a very wide dynamic range because of the extreme values of capacitance and loss they exhibit at different temperatures and electrical frequencies. Measurement of the dielectric permittivity (capacitance) and dielectric loss of KTN and KDP samples vs. temperature is made using the capacitance bridge described in Appendix D. The dielectric samples tested are prepared by following the steps described in Chapter 5. The capacitative-devices are then mounted on a temperature-controlled platform in a light-tight vacuum cryostat that can reach temperatures as low as 85K.

Table 7.1. Samples used in Capacitative measurements.

Crystal	Origin	Sample	Contacts	Size
KDP	LLNL (Advanced Lasers Group)	CT-01	Pd:Au	711μm x 9.45mm^2
		CT-03		215μm x 3.53mm^2
KTN	Rytz (PK9)	KTN01	Cr:Au (200:1400Å)	315μm x 2.25mm^2
		KTN02		
		KTN05		137μm x 1mm^2
	Rytz (unknown)	KTN03		1mm x 13.5mm^2
		KTN03A		1mm x 8.12mm^2
		KTN03B		1mm x 4.56mm^2
	Rytz (PK15)	KTN04A		60μm x 1mm^2
		KTN04B		
		KTN04D		
		KTN04E		

Figure 7.1 shows a plot of the dielectric permittivity as a function of temperature for sample CT-01. The dielectric permittivity is obtained through measurements of the capacitance of the sample using an A.C. measurement frequency and amplitude of 20Hz and 2.8V, respectively. The shape of this curve is typical of KDP material and arises from changes in the dielectric permittivity as the Curie temperature is traversed. Fitting the data in the paraelectric phase results in the Curie-Weiss temperature (Ø) of 118.1K and a Curie constant (C) of 3252 K. In order to gauge how sharp the transition is, a plot was made of the derivative of the dielectric permittivity as a function of temperature for KDP sample CT-01 (see Figure 7.2). The paraelectric-to-

ferroelectric transition for this KDP sample occurs at 119.2K and is about a few tenths of a degree wide. Other samples taken from the same KDP crystal have nearly identical transition temperatures, Curie constants, and Curie-Weiss temperatures. The dielectric loss ($\mathfrak{D} = \varepsilon''/\varepsilon'$) of KDP sample CT-01 is plotted in Figure 7.3 as a function of temperature. Values for the real part of the dielectric constant are shown in Figure 7.1. Values for the imaginary part of the dielectric constant are obtained from simultaneous measurement of the sample resistance. At the Curie temperature the loss drops more than two orders of magnitude below values at temperatures below the Curie temperature.

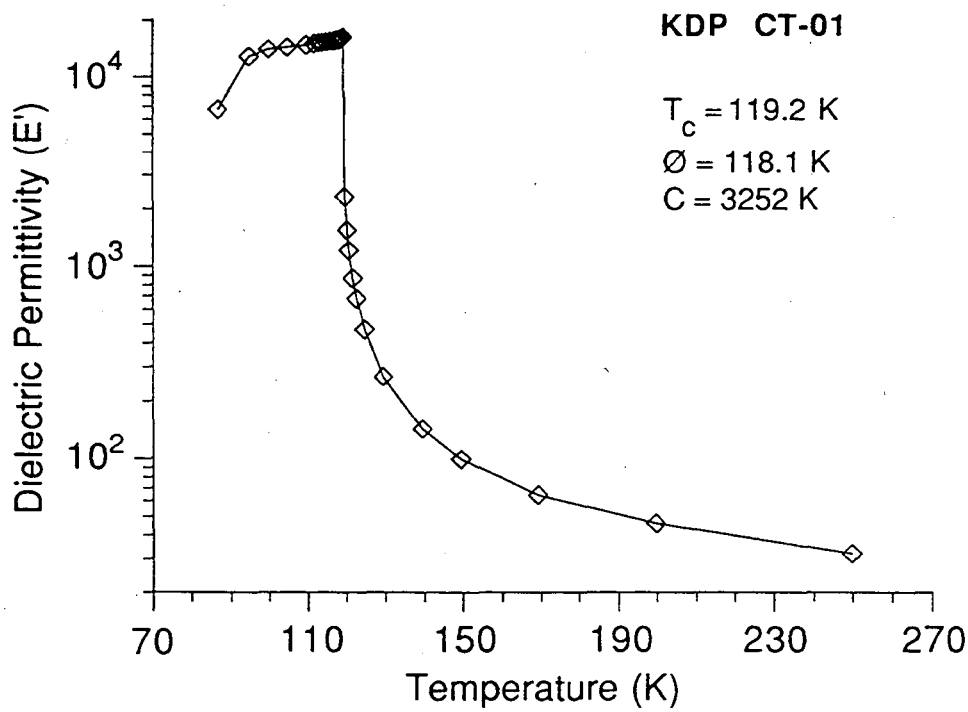

Figure 7.1. Dielectric permittivity vs. temperature of KDP sample CT-01 measured with a 20Hz 2.8V A.C. signal.

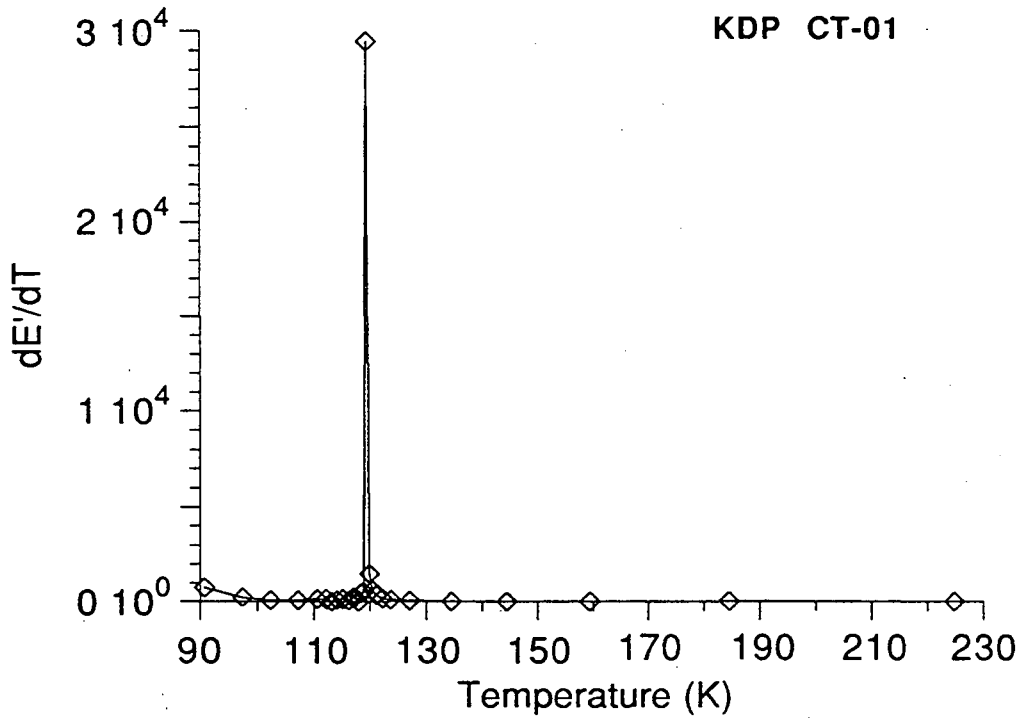

Figure 7.2. Derivative of the dielectric permittivity (from Figure 7.1) vs. temperature.

Figure 7.4 compares two plots of KDP sample CT-03 as a function of temperature with and without an applied D.C. bias. Both plots were made with a 20Hz 2.8V A.C. signal. The difference in the height of the two curves is due to the non-linearity of the dielectric permittivity (see Chapter 2). With the application of an applied bias, the slope (dielectric permittivity) of the electric displacement vs. electric field curve is shallower and thus a plot of the dielectric permittivity vs. temperature is depressed. In the paraelectric region, above the transition peak, the two curves do not differ noticeably indicating a nearly linear dielectric permittivity.

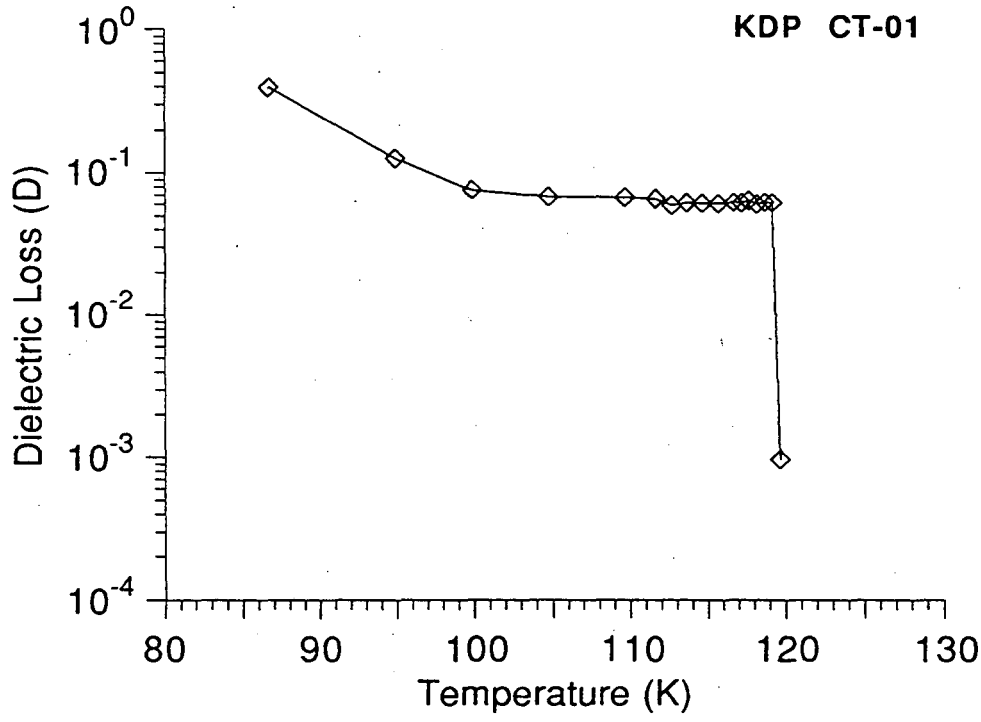

Figure 7.3. Dielectric loss vs. temperature of KDP sample CT-01 measured with an A.C. sinusoidal signal of 20Hz and 2.8V.

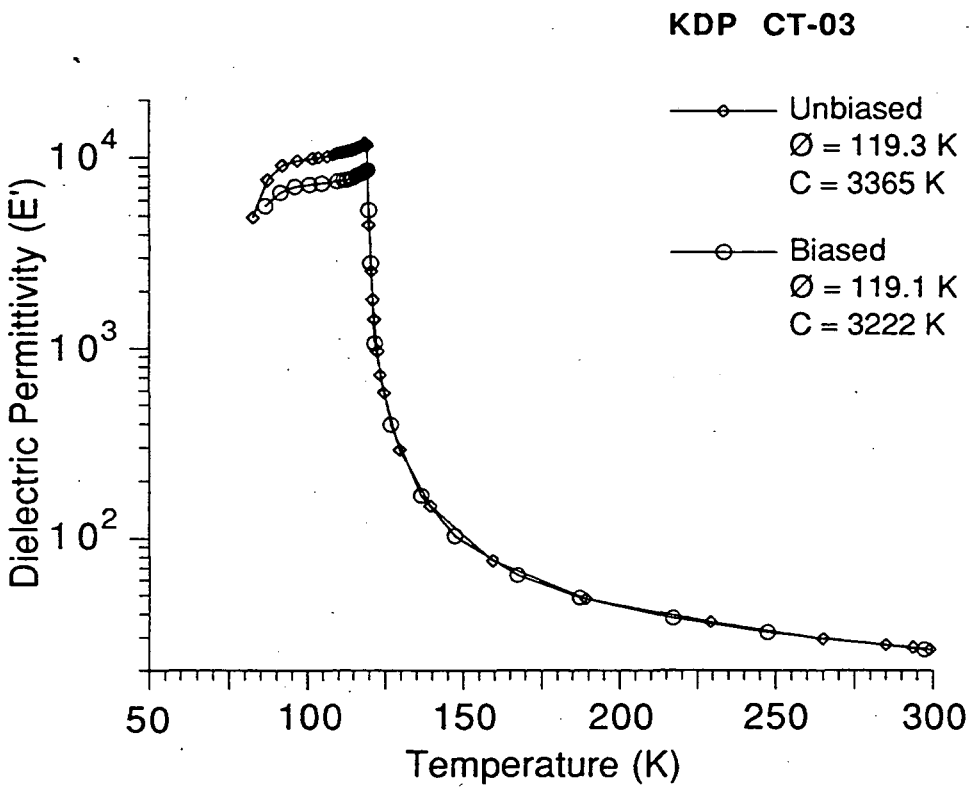

Figure 7.4. Dielectric permittivity vs. temperature for KDP sample CT-03 measures with a 20Hz 2.8V A.C. signal without D.C. Bias and with a 20V applied D.C. Bias.

Figure 7.5 shows a plot of the dielectric permittivity vs. temperature for KTN sample KTN-05 measured with a 20Hz, 1.4V A.C. measuring signal. The three peaks at 132.1, 144.8, and 160.6 Kelvin correspond to the two ferroelectric-to-ferroelectric transitions and the ferroelectric-to-paraelectric transition of alloyed KTN, where x = 0.19 (Eq. 4.1 and Figure 4.3). Fitting the paraelectric region with the Curie-Weiss law, the Curie-Weiss temperature and Curie constant are found to be 164.1 K and 12.1 x 10^4 K, respectively. KTN samples KTN-01 and KTN-02 are from the same crystal as KTN-05 but the transition peaks are shifted approximately 0.1° toward lower and 4.4° toward

higher temperatures, respectively. In addition, their Curie-Weiss temperatures and Curie constants differ: 173.6 K and 8.9 x 10^4 K for KTN-01, and 174.1 K and 9.5 x 10^4 K for KTN-02. These small differences are attributed to the differences in composition between samples. Figure 7.6 shows the corresponding dielectric loss as a function of temperature of KTN-05. At each transition there is a dip in the loss. At the ferroelectric-to-paraelectric transition (T_c ~ 160.6K) the loss gradually decreases by approximately one order of magnitude.

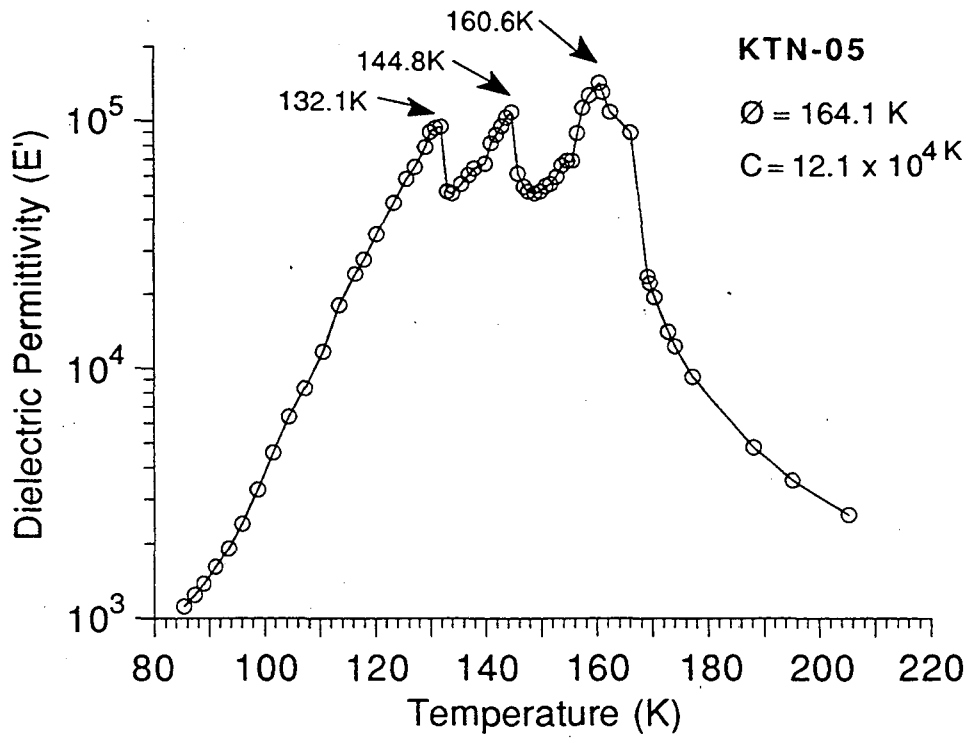

Figure 7.5. Dielectric permittivity vs. temperature of KTN sample KTN-05 measured with a 20Hz 1.4V A.C. signal. The rhombohedral-orthorhombic, orthorhombic-tetragonal, tetragonal-cubic transitions occur at 132.1, 144.8, and 160.6 Kelvin, respectively.

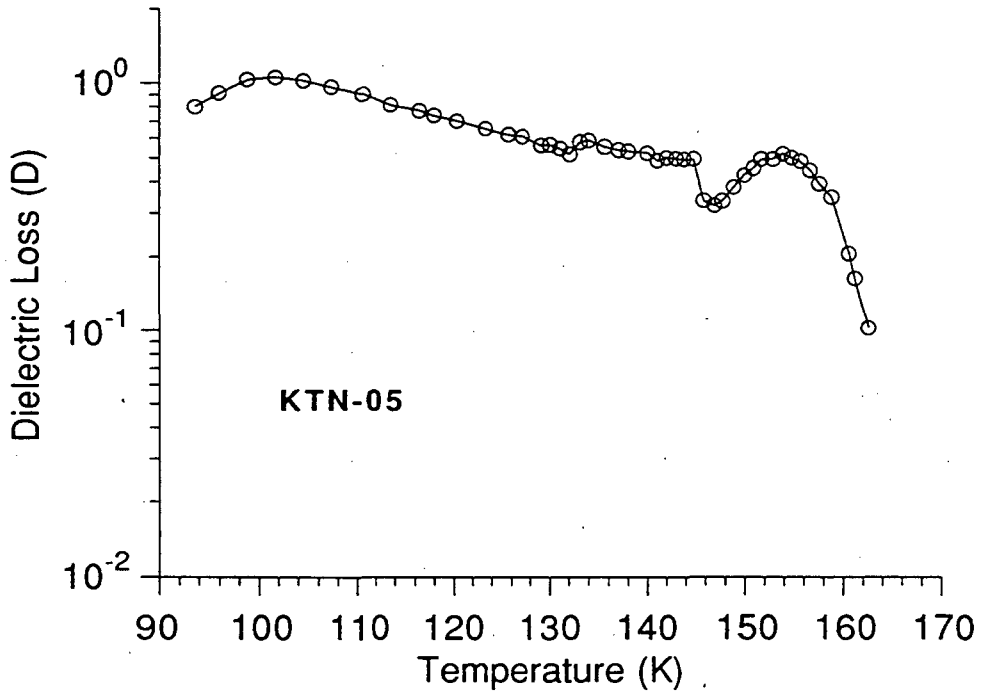

Figure 7.6. Dielectric loss vs. temperature of KTN sample KTN-05 measured with a 20Hz 1.4V A.C. signal.

Figure 7.7 shows the dielectric permittivity of sample KTN-04D as a function of temperature. The observed peak is composed of three transition peaks but because of the proximity of the transitions and inhomogeneities in the crystal they spread into one diffuse peak. The peak is at approximately 68.9K and is much broader than the peaks observed in KDP material. Fitting the higher temperature slope of the data to the Curie-Weiss law results in a Curie-Weiss temperature of 88.5 K and a Curie constant of 8.45×10^4 K indicating that the fraction of tantalate is approximately $x = 0.8$. Samples KTN-04A, KTN-04B, and KTN-04E are all from the same crystal. Dielectric measurements result in the following Curie-Weiss temperatures and Curie constants, respectively:

88.7, 90.1 and 88.6 K, and 8.5 x10^4, 8.6 x 10^4 and 7.3 x 10^4 K. Taking the derivative of the dielectric constant as a function of temperature results in the plot of Figure 7.8. The two broad peaks indicate a flatter temperature response of the dielectric constant in comparison with KDP.

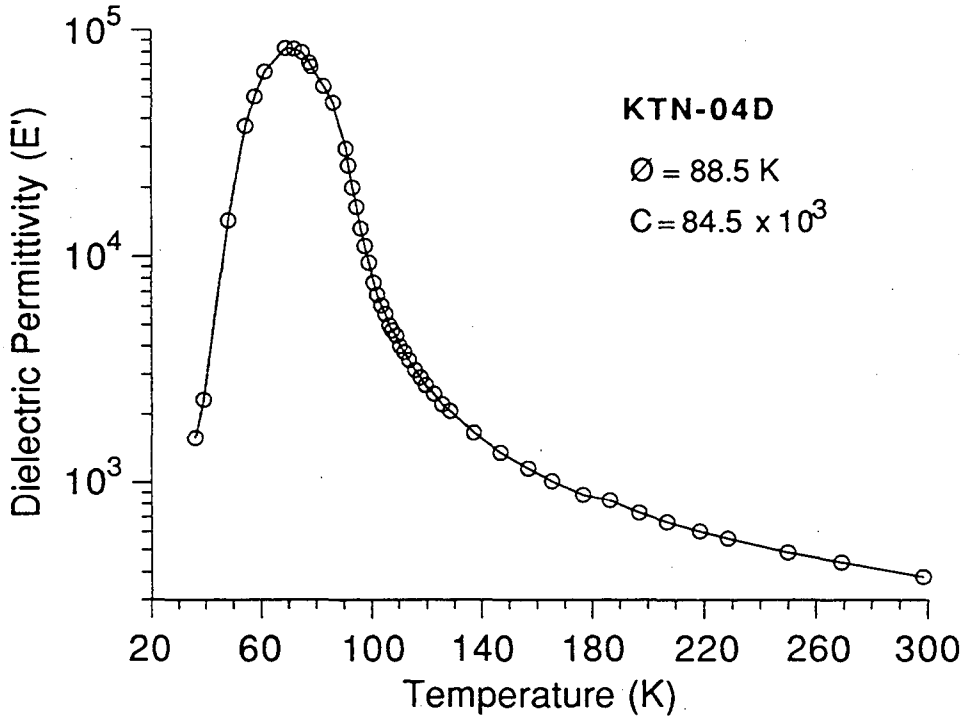

Figure 7.7. Dielectric permittivity vs. temperature for KTN sample KTN-04D measured with a 20Hz 2.4V A.C. signal.

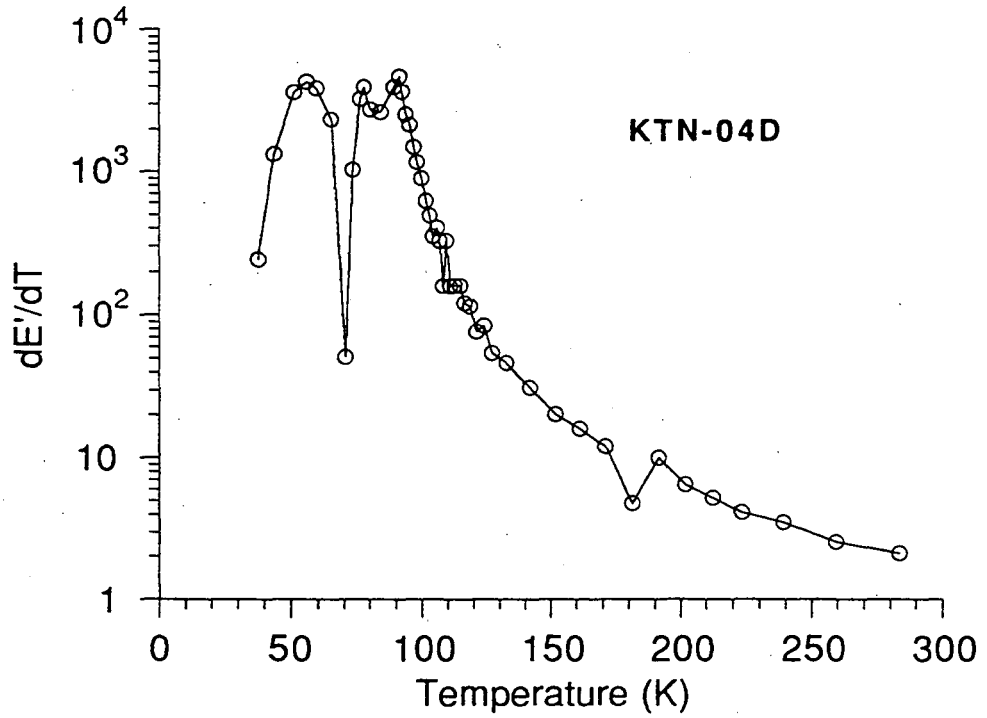

Figure 7.8. Derivative of the absolute value of the dielectric permittivity (from Figure 7.8) vs. temperature for sample KTN-04D.

7.2 Response Measurements

Variable temperature and frequency measurements of the response of KDP and KTN detectors were made by our collaborators at the NASA Ames Research Center. All devices were prepared according to the sample preparation described in Chapter 5 and device mounting and wiring procedures described in Chapter 6. Table 7.2 lists the devices tested along with their dimensions, contact metals and thickness, contact wire and size, the theoretical thermal time constant, and detectivity.

Table 7.2. Devices tested for Response.

	KDP		KTN		
	DET-02	ET-07	KTN-04C	KTN-04B	KTN-04E
Area	0.25mm^2	0.25mm^2	1mm^2	1mm^2	1mm^2
Thickness	25μm	25μm	60μm	60μm	60μm
Contact Metal Thickness-Å	Pd:Au 200:1400	Pd:Au 200:1400	Cr:Au 200:1400	Cr:Au 200:1400	Cr:Au 200:1400
Contact Wire # - size - type	2 - 1/2 mil x 3mm - Br	2 - 1/2 mil x 3mm - Br	2 - 2mil x 3mm - Cu	4 - 8mil x 3mm -.Cu	4 - 8mil x 3mm -.Cu
Absorbing layer		Krylon Spray Paint			Epoxy-Carbon
Thermal time constant using (η = 1)	1.8 s (121K)	1.8 s (121K)	0.1 s (87K)	0.0032 s (87K)	>0.0032 s (87K)
Theoretical Detectivity (Hz$^{1/2}$/W) using (η = 1)	5.51 x 10^{11} (121K)	5.51 x 10^{11} (121K)	5.93 x 10^{10} (87K)	1.07 x 10^{10} (87K)	1.07 x 10^{10} (87K)

Response vs. temperature measurements were made using a chopping frequency of 15Hz in conjunction with a standard blackbody at 1000K (peak $\lambda \approx .3\mu m$) to form the infrared source. Figure 7.9 shows the voltage response as a function of temperature of KDP detector DET-02 under 8V of D.C. bias. The peak response occurs at 121.1 K and is 2889 V/W. KDP detector ET-07, shown in Figure 7.10, was coated with a "Krylon Flat Black Spray Paint" in an attempt to increase the absorption of the device and thus the responsivity. The peak

response for ET-07 is 122V/W and occurs at 120.7 K. Instead of increasing the responsivity, the application of the Krylon spray paint absorbing layer resulted in a decreased responsivity. The most probable cause of this decrease in responsivity is an increase of the total heat capacity of the device, which shifts the response vs. frequency curve to the left, effectively decreasing the response at the measuring frequency of 15 Hz.

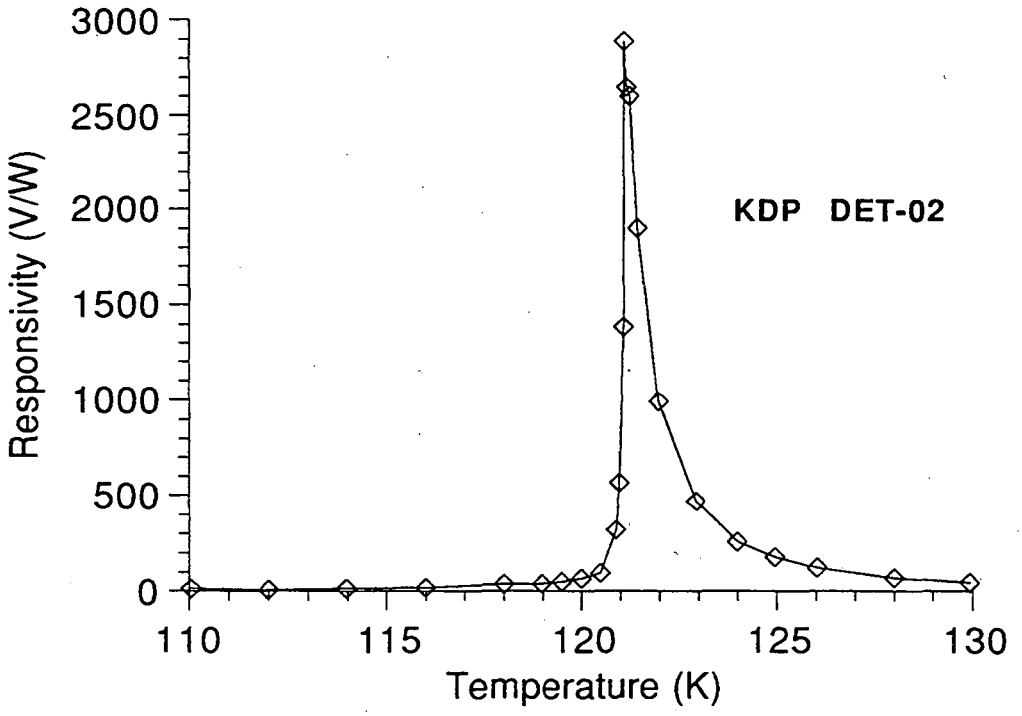

Figure 7.9. Responsivity vs. temperature for KDP detector DET-02 under 8V D.C. bias with a 15 Hz chopping frequency and 1000 K blackbody infrared source.

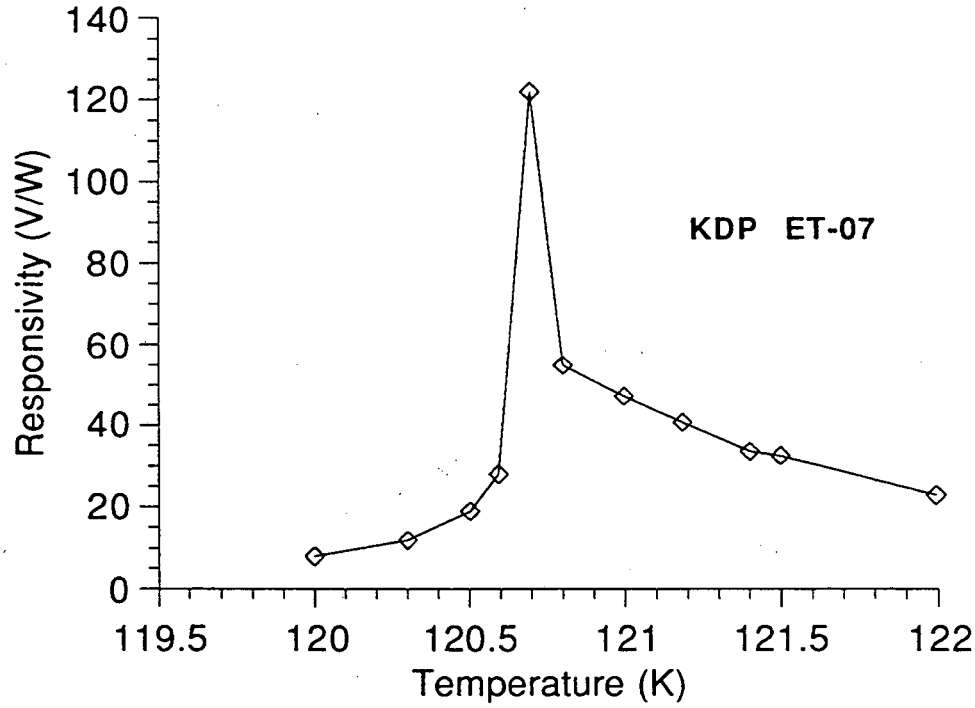

Figure 7.10. Responsivity vs. temperature for "Krylon Flat Black" spray painted KDP detector ET-07 under 8V D.C. bias with a 1000 K blackbody chopped at 15 Hz.

Figure 7.11 shows the responsivity vs. temperature for KTN detector KTN-04C with an applied D.C. bias of 8V. There are two response peaks occurring at 87 K and 35 K. The smaller of the two peaks occurs just below the Curie-Weiss temperature, 88.5 K. The larger of the two peaks occurs well below the Curie temperature and its origin is unknown. It may come from a decrease in dielectric loss or an increase in the pyroelectric coefficient. Nevertheless, both peaks are broader than the KDP peaks requiring less stringent temperature control during detector operation.

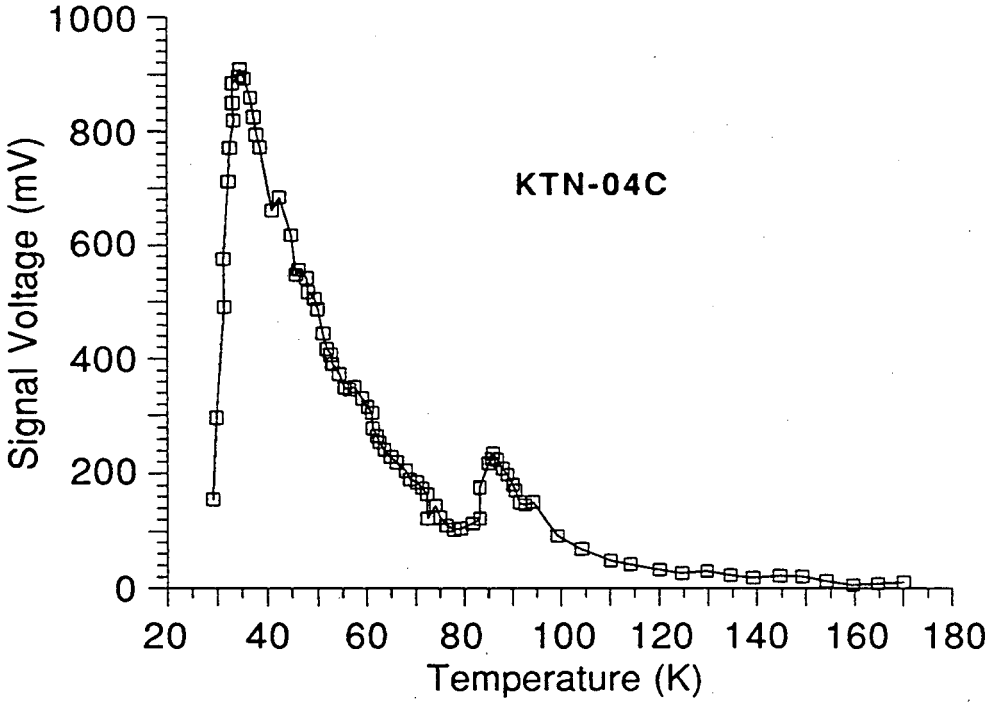

Figure 7.11. Relative response vs. temperature for KTN detector KTN-04C under 8V D.C. bias with a 1000 K blackbody infrared source chopped at 15 Hz.

The addition of an absorbing layer makes it difficult to determine the effectiveness of the absorbing layer independent of the increase in heat capacity of the detector. To determine the two parameters independently, two KTN detectors, KTN-04B and KTN-04E, were made identically except that one had an absorbing layer (epoxy carbon recipe, see Section 6.3) and the other did not. The devices were purposely made thermally "fast" by connecting the detector with four 8-mil copper wires to the heat sink. These devices allowed measurement of the flat top frequency response shown in Figure 7.12. A shift in the thermal roll-off is a function of a change in the specific heat of the device, and a shift in height of the plateau indicates a change in the device emissivity.

The absorbing layer increases the signal vs. frequency height by 15.3 times and shifts it to the left by 1.25 times. This indicates both an increase in emissivity and specific heat of the device (see Section 6.2, Table 6.1 and Figure 6.7).

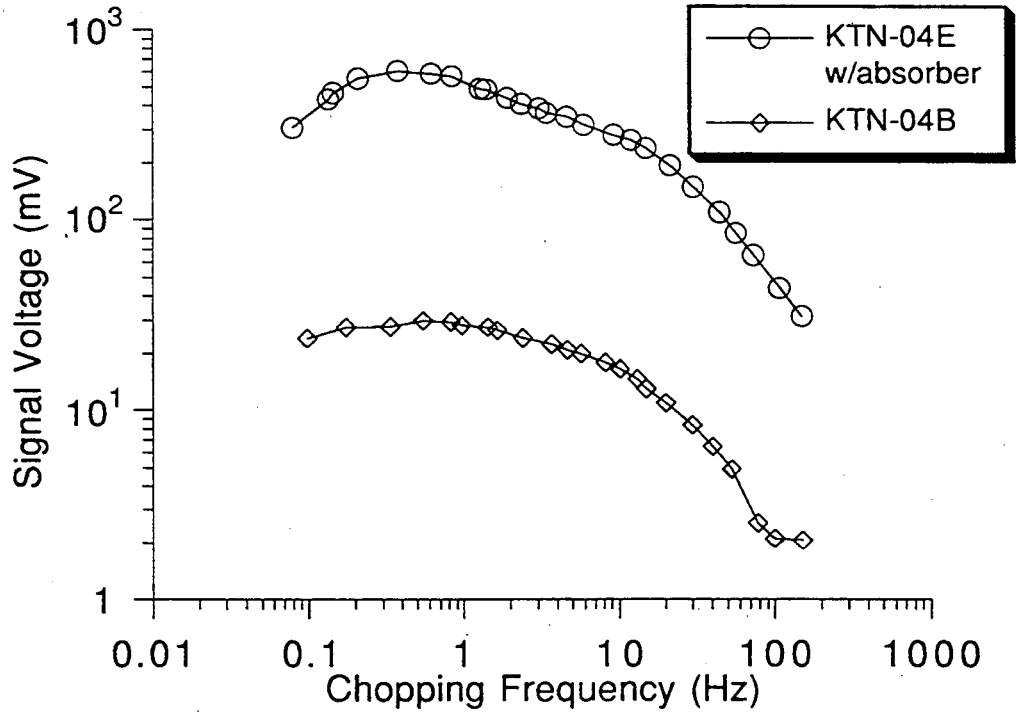

Figure 7.12. Signal voltage vs. chopping frequency for two KTN detectors, one with an applied epoxy - carbon absorbing layer, KTN-04E, and the other without, KTN-04B. Both measurements used a 1000 K blackbody as an infrared source.

8. CONCLUSION

KDP and KTN ferroelectric materials have been processed and their dielectric properties and response to infrared radiation characterized. Despite KDP's higher response, KTN emerges as a clear choice for future pyroelectric detector research. One primary disadvantage associated with KDP is the narrow temperature range over which maximum response is observed. In addition, KDP's hygroscopic nature makes it difficult to process and leaves uncertainty regarding its stability during long-term missions. Also, KDP's response peak occurs at ~ 120 K. The desired detector operating temperature is ~ 100 K; lower operating temperatures result in lower background radiation leading to higher detectivity. Although other materials in the KDP family have Curie temperatures and, thus, peak responsivities closer to 100 K, they are also hygroscopic.

KTN's advantages include a broader pyroelectric response, the ability to tailor composition for peak response at 100 K, and ceramic-like properties that make it much easier to process. Unfortunately, KTN's response peak is much lower than KDP's. However, the KTN devices tested are 10 times greater in volume than the KDP devices tested; the heat capacity of the KTN devices is larger. The detector response is greater for higher emissivity, higher pyroelectric coefficient, and lower heat capacity. The emissivity of the detector is increased by applying a black absorbing layer. In addition, the effective emissivity can be increased by fabricating composite pyroelectric bolometers. The pyroelectric coefficient is increased by D.C. biasing the detector during operation. Also, other materials may be found that have higher pyroelectric coefficients and/or lower specific heats. The heat capacity is reduced by decreasing the detector thickness, area and specific heat. Decreasing the

thickness of the detectors can be accomplished through more advanced polishing techniques or through thin-film growth.

Ongoing investigations aim at improving the performance of the KTN pyroelectric detector and looking for other ferroelectric materials with more desirable properties than those of KTN. Future work in KTN will concentrate on increasing the IR absorption of KTN pyroelectric devices, reducing the size of the detectors, and characterizing its spontaneous polarization and response to d.c. bias by measuring its hysteresis loops. Recent advances in thin-film growth of perovskite superconducting materials by pulsed laser deposition makes this a viable technique to apply to thin film growth of KTN.[64] Investigators at the Bell Communications Research Laboratory have been successful in growing stoichiometric KTN.[65] Hysteresis measurements will enable determination of the origin of the large lower-temperature response peak observed in the KTN devices.

9. REFERENCES

1. R.A. Hanel, J. Opt. Soc. Am. **51**, 220-224 (1961).

2. J. Cooper, Rev. Sci. Instrum. **33**, 92-95 (1962).

3. J. Cooper, J. Sci. Instrum. **39**, 467-472 (1962).

4. M.Y. Pines, "Characteristics of Potassium Tantalate Niobate as a Pyroelectric Detector," M.S. Thesis, University of California at Los Angeles (1971), 1-2.

5. R.W. Whatmore, Rep. Prog. Phys. **49**, 1340 (1986).

6. G.S. Hubbard, R.E. McMurray, Jr., R.P. Hanel, D.E. Dominguez, F.P.J. Valero, H.B. Baumann, W.L. Hansen and E.E. Haller, "Pyroelectric Detector Development for the Radiation Measurement System", Proceedings of the Fourth Symposium on Global Change Studies, January 17-22, 1993.

7. G.S. Hubbard, R.E. McMurray, Jr., R.P. Hanel, D.E. Dominguez, H. Chang and E.E. Haller, "High D* Pyroelectric Detectors for Operation Near 100K", Proceedings of the Innovative Long-Wavelength Infrared Detector Workshop,April 7-9, 1992.

8. Lines & A. Glass, *Principles and Applications of Ferroelectrics and Related Materials* (Clarendon Press, Oxford, 1977), 562.

9. [5], 1365-6.

10. S. Nomura, M. Mizuno, J. Kuwata, M. Abe, and J.C. Burfoot, Ferroelectrics **51**, 3-8 (1983).

11. [4]

12. [5], 1339.

13. [8], 35.

14. [5], 1337.

15. J.W. Morris, Jr., *Engineering 45 Class Notes* (Department of Materials Science and Mineral Engineering, 1992), 475-6.

16. [8], 566.

17. Burfoot & Taylor, *Polar Dielectrics and their Applications* (University of California Press, Berkeley and Los Angeles, 1979), 35.

18. [17], 2.

19. [8], 608.

20. [8], 479.

21. [17], 8-9.

22. [5], 1339.

23. [17], 9.

24. [15]., 478.

25. [15], 493.

26. J.S. Blakemore, *Solid State Physics*, (W.B. Saunders Company, Philadelphia, 1969), 352.

27. [17], 238.

28. G.A. Smolenski, *Ferroelectrics and Related Materials*, (Gordon and Breach Science Publishers, Amsterdam, 1984), 366-7.

29. [8], 103.

30. [8], 9.

31. [17], 35.

32. A.F. Devonshire, "Theory of Ferroelectrics," *Advances in Physics* **3** (10), 94 (1954).

33. [5], 1338-9.

34. [5], 1341.

35. [17], 383.

36. A. Beer, "Infrared Detectors," p 259-85.

37. F. Kreith and M.S. Bohn, "Principles of Heat Transfer," Harper & Row, New York, p 4-12, 1986.

38. [5], 1341-3.

39. [8], 565.

40. [5], 1345.

41. [8], 565.

42. [8], 565.

43. [36], 268.

44. [5], 1347.

45. [5], 1348.

46. [8], 565.

47. [5], 1348.

48. [5], 1344.

49. [36], 274

50. T. Mitsui, et. al., *An Introduction to the Physics of Ferroelectrics*, (Gordon and Breach, New York, 1976).

51. J. Wang, Q. Guan, Y. Liu, J. Wei, D. Wadi, Y. Lian, H. Yang, and P. Ye,..Appl. Phys. Lett. 61 (23), 2761 (1992).

52. [32].

53. [8], 293-5.

54 G.A. Smolenski, *Ferroelectrics and Related Materials*, (Gordon and Breach Science Publishers, Amsterdam, 1984), 21-23.

55. [50], 227-230.

56. [8], 241-4.

57. [54], 18-21.

58. D. Rytz and H.J. Scheel, J. Crystal Growth **59**, 470 (1982).

59. W.D. Nesse, *Introduction to Optical Mineralogy*, 51-3, 63-4.

60. [36]. 275-281.

61. R.M. Gibbons, *Thermophysical Data for Cryogenic Materials*, LBL Report UCRL-3421, p. 678-9.

62. G.K. White, *Experimental Techniques in Low-Temperature Physics*, p. 320, 1979.

63. W. Kanzig, *Ferroelectrics and Antiferroelectrics* (Academic Press, New York, 1957), p. 61.

64. C. M. Cotell and K.S. Grabowski, MRS Bulletin **XVII** (2), 44-53 (February 1992)

65. S. Yilmaz, T. Venkatesan and R. Gerhard-Multhaupt, Appl. Phys. Lett **58** (22), 2479-81 (1991).

APPENDIX A. The 32 crystallographic point groups arranged by crystal systems

Crystal System	Symbol	Pyroelectric	Piezoelectric
Triclinic	1	√	√
	$\bar{1}$		
Tetragonal	4	√	√
	$\bar{4}$		√
	4/m		
	422		√
	4mm	√	√
	$\bar{4}$2m		√
	4/mmm		
Hexagonal	6	√	√
	$\bar{6}$		√
	6/m		
	622		√
	6mm	√	√
	$\bar{6}$m2		√
	6/mmm		
Monoclinic	2	√	√
	m	√	√
	2/m		
Orthorhombic	222		√
	mm2	√	√
	mmm		
Trigonal	3	√	√
	$\bar{3}$		
	32		√
	3m	√	√
	$\bar{3}$m		
Cubic	23		√
	m3		
	432		
	$\bar{4}$3m		√
	m3m		

A tick (√) indicates that the point group is pyroelectric or piezoelectric, as the case may be.

APPENDIX B. Thermal Conductivity vs. Temperature data for various metals. (References 61 and 62)

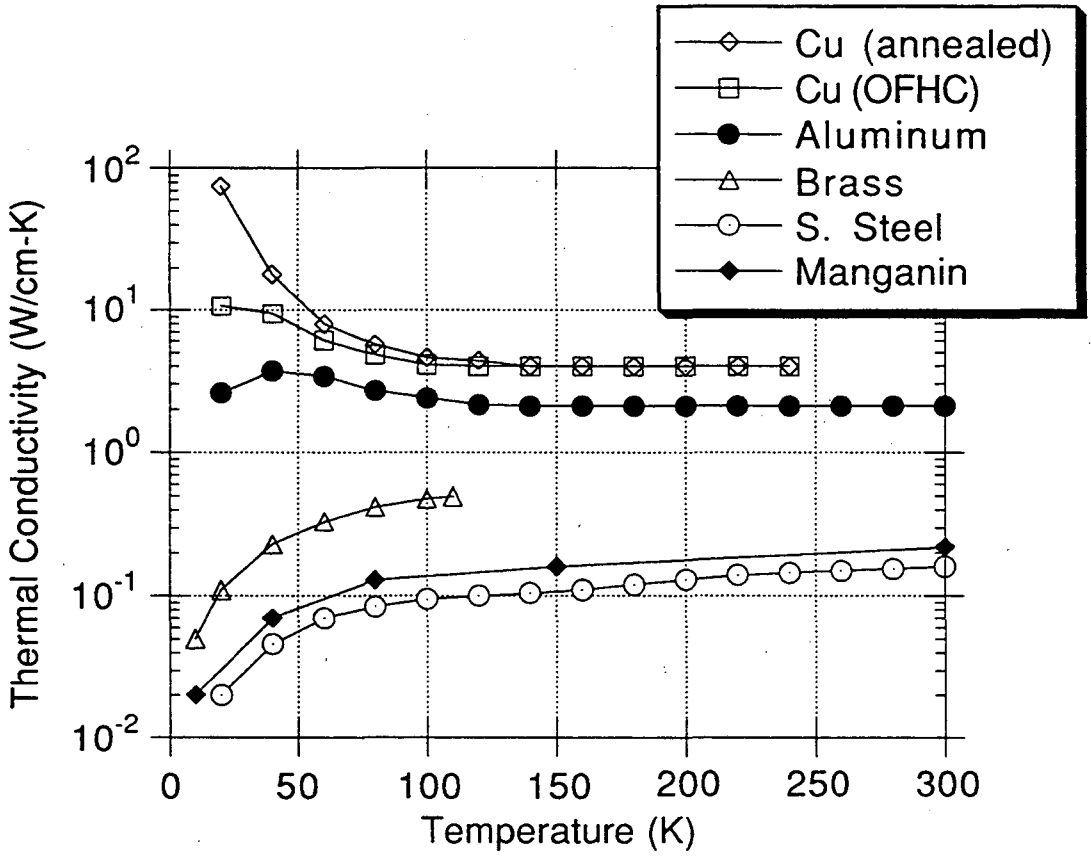

APPENDIX C. Specific Heat of KDP (Reference 63)

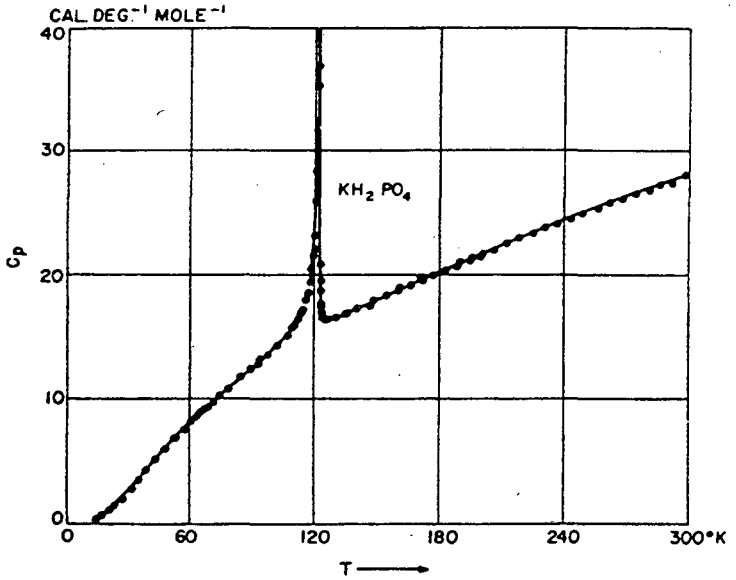

APPENDIX D. Capacitance Bridge

The schematic of the capacitance bridge is shown on the following page. A Princeton 5301 Lock-in Amplifier is used both to provide the A.C. measurement signal and to differentiate between the measured signals at A and B. When the phase and amplitude of the signal at A exactly matches that at B, the bridge is balanced. Balancing is performed by adjusting the variable resistor (R_1) and capacitor (C_3). At the balanced condition there is an impedance balance between the four arms of the bridge which allow one to solve for the parallel or series resistance (R_S) and capacitance (C_S) of the sample under test. In the parallel case:

$$C_S = \frac{C_1 C_3}{C_2} \qquad [7.1]$$

$$R_S = \frac{C_2 R_1}{C_1}, \qquad [7.2]$$

which is valid for the KDP and KTN samples tested. The dielectric permittivity can be solved for by using Eq. 2.1, and the dielectric loss for the parallel modeled condition is simply $D = (\omega RC)^{-1}$. This procedure is performed at various temperatures resulting in plots of the dielectric permittivity and dielectric loss as a function of temperature.

This capacitance bridge is capable of variable frequency measurements ($15Hz < f < 1kHz$) of the capacitance and parallel resistance of the sample under test. Large values of loss, $D > 0.1$, indicate a high-loss material and $D < 0.01$ represent a low-loss material. In the parallel mode the bridge has a dynamic range of $3pF < C_S < 7nF$ and $3 \times 10^{-7} < D < 3.1 \times 10^4$. In addition, by altering the capacitors and/or resistors this range can be shifted or expanded to encompass more extreme values.

LAWRENCE BERKELEY LABORATORY
UNIVERSITY OF CALIFORNIA
TECHNICAL INFORMATION DEPARTMENT
BERKELEY, CALIFORNIA 94720

ABH239
LBL Libraries